EUROPEAN ORGANIZATION FOR NUCLEAR RESEARCH

CERN-EP/87-166
14 September 1987

THE BEAM AND DETECTOR FOR A HIGH-PRECISION MEASUREMENT OF CP VIOLATION IN NEUTRAL-KAON DECAYS

H. Burkhardt*), P. Clarke, D. Cundy, N. Doble, L. Gatignon, R. Hagelberg, G. Kesseler,
J. van der Lans, I. Mannelli**), T. Miczaika***), H.G. Sander†), A.C. Schaffer†), P. Steffen††),
J. Steinberger, H. Taureg, H. Wahl and C. Youngman†††)
CERN, Geneva, Switzerland.

G. Dietrich×), F. Eisele††) and W. Heinen××)
Institut für Physik, Univ. Dortmund, Fed. Rep. Germany+).

R. Black, D.J. Candlin, J. Muir, K.J. Peach, B. Pijlgroms×××),
I.P. Shipsey#) and W. Stephenson
Phys. Dept., Univ. Edinburgh, UK+).

H. Blümer, M. Kasemann, K. Kleinknecht, B. Panzer and B. Renk
Institut für Physik, J. Gutenberg Univ., Mainz, Fed. Rep. Germany+).

E. Auge, R.L. Chase, M. Corti##), D. Fournier, P. Heusse and A.M. Lutz
LAL, Univ. Paris Sud, Orsay, France+).

A. Bigi, M. Calvetti, R. Carosi, R. Casali, C. Cerri, R. Fantechi, S. Galeotti, E. Massa,
A. Nappi, D. Passuello and G. Pierazzini
Istituto di Fisica and Sezione INFN, Pisa, Italy+).

C. Becker, D. Heyland***), M. Holder, G. Quast, M. Rost, W. Weihs and G. Zech
Fachbereich Physik, Universität-Gesamthochschule, Siegen, Fed. Rep. Germany+).

(Submitted to Nucl. Instrum. Methods in Phys. Research)

---

*) Present address: Fachbereich Physik, Univ. Siegen, Fed. Rep. Germany.
**) Present address: Istituto di Fisica and Sezione INFN, Pisa, Italy.
***) Present address: Deutsche Forschungs- und Versuchsanstalt für Luft- und Raumfahrt, Cologne, Fed. Rep. Germany.
†) Present address: LAL, Univ. Paris Sud, Orsay, France.
††) Present address: DESY, Hamburg, Fed. Rep. Germany.
†††) Present address: II. Inst. für Exp. Physik der Univ. Hamburg, Fed. Rep. Germany.
×) Present address: Robert Bosch GmbH, Nuremberg, Fed. Rep. Germany.
××) Present address: H.T. Heinen & Thux, Koblenz, Fed. Rep. Germany.
×××) Present address: FVI, Univ. Amsterdam, The Netherlands.
#) Present address: Syracuse University, Syracuse, NY, USA.
##) Present address: Ars, Milan, Italy.
+) See Acknowledgements.

ABSTRACT

The K^0 beam and detector used for a high-precision measurement of the CP-violation parameter ϵ' at the CERN Super Proton Synchrotron (SPS) are described. The beam provides K_L and K_S alternately through a common decay region. The detection of the decays is based on wire chambers and calorimeters without employing a magnet. The trigger and readout system achieve a high selectivity for the suppressed, CP-violating, two-pion decays of the K_L by incorporation of hard-wired processors. The readout is based on FASTBUS for maximum data rates.

1. INTRODUCTION

Recent years have seen a renewed interest in the study of CP violation from both the theoretical and experimental points of view [1]. The higher energy available at accelerators, and the advances in detectors and electronics, permit a considerable improvement in the accuracy of measurement of some of the parameters describing CP violation in kaon decays. This may help to clarify the origin of CP violation, and in particular it will allow more sensitive checks of the Standard Model.

An important parameter, ϵ'/ϵ, can be determined by comparing the rates of the two-pion decay modes of the neutral kaons K_L and K_S. Specifically the relation is: $1 - 6|\epsilon'/\epsilon| \approx |\eta_{00}/\eta_{+-}|^2$, where η_{00} is the ratio of the amplitudes K_L to K_S in the $\pi^0\pi^0$ decay and η_{+-} is the corresponding ratio in the $\pi^+\pi^-$ decay. This double ratio is known to deviate from unity by no more than a few percent [2]. The systematic requirements are therefore quite severe.

In the experiment [3] there are two different running modes: the K_L beam and the K_S beam. The $\pi^0\pi^0$ and $\pi^+\pi^-$ decays are detected simultaneously in each mode. Since the K_L beam generates a nearly uniform distribution of decays along the 50 m decay region, a movable K_S target station is used to generate a comparable distribution of K_S decays (typical decay length $\approx$ 5 m) throughout that region. Neutral decays are measured with a lead/liquid-argon calorimeter. Charged decay tracks are observed with wire chambers, and the energy is measured by the combination of the liquid-argon calorimeter and an iron/scintillator hadron calorimeter. The overall layout of the experiment is shown in Figs. 1a,b.

In the case of K_L, the two-pion modes represent only a small fraction of the decays. In order to maximize the number of K_L two-pion decays written to tape, it is necessary to have fast data processing and a high level of on-line rejection of three-body decays. The trigger makes use of scintillation counters, fast information from detector elements, a hard-wired processor, and two IBM 168 emulators (168E). The data-acquisition system employs FASTBUS, the 168Es and a VAX 750 computer.

This paper describes in detail the construction and performance of the beam and detectors. The order of presentation is: i) the beam, ii) the scintillation counters and hodoscopes, iii) the wire chambers, iv) the calorimeters, v) the trigger system, and vi) the data-acquisition system.

2. K_L AND K_S BEAMS

The beam layout is designed to provide collinear beams of either K_L or K_S entering a common, evacuated decay region leading to the experimental detectors. The two beams are produced by directing primary protons at 450 GeV/c onto targets located at different longitudinal positions in the experimental hall. The beam elements are constructed so as to allow alternation between the two modes at regular intervals. The principal parameters of the two beams are given in Table 1.

2.1 K_L beam

The K_L beam originates from a target station at the entrance to the experimental hall. The layout of the target station together with the first section of the beam is shown schematically in Fig. 2. The target head consists of a series of four beryllium rods, each 100 mm in length and 2 mm in diameter. These are accurately aligned along the axis of the kaon beam and suspended at each end by aluminium foils, 25 μm thick. The target assembly is motorized so that either the target or an empty position can be presented to the proton beam.

The last bending magnet upstream of the target allows the direction of the incident proton beam to be inclined in the vertical plane. At the chosen production angle of 3.6 mrad the flux of neutrons relative to kaons in the beam is about 8:1. The target is followed by an initial, 1.6 m long, mobile collimator, designed to reduce the angular acceptance for secondary particles. A vertical sweeping magnet, of 10.8 T·m bending strength, then deflects the primary proton beam further downwards and deviates charged secondaries and decay muons away from the neutral beam line. At the end of a laterally shielded drift length of 3.2 m, there is a second mobile beam-dump/collimator which absorbs the remaining primary protons and other charged particles, and which again reduces the acceptance of the neutral beam. The bulk of each of these beam-dump/collimator units is composed of iron blocks, which are fitted with tungsten alloy inserts to minimize the absorption length for hadrons and hence reduce the yield of muons. Both the proton beam transport to the target and this first 16 m section of the K_L beam are shielded to permit a nominal intensity of 1×10^{11} 450 GeV/c protons on target per SPS pulse, every 14.4 s.

From this first section onwards, the neutral beam is transported in vacuum over its full length and finally passes through a central hole in the detectors before being absorbed in a beam dump, 252 m from the target. This vacuum, typically 3×10^{-3} Torr, reduces K_L elastic scattering, K_S regeneration, and neutron-induced K^0 generation to levels lower than the 10^{-5} level. The final angular acceptance of the beam (± 0.2 mrad opening angle) is defined by a fixed, 1 m long collimator with a tapered bore lined with tungsten, located 48 m after the target. This is preceded and succeeded by horizontal sweeping magnets. The beam line subsequently passes through the vertical bending magnets of the K_S beam train, described below, which is stationed in its most upstream position during K_L running and set so as to present no obstacle to the K_L beam. The train carries a final collimator with an aperture larger than the K_L beam acceptance, located 120 m after the target. This is designed to prevent particles produced at the edges of the defining collimator from reaching the sensitive area of the detectors.

Typical counting rates recorded by the detectors with the K_L beam are indicated in Table 2.

2.2 K_S beam

For the K_S beam, the primary proton beam is first attenuated by passing it through 1.6 m of beryllium absorber, and is subsequently collimated to a nominal intensity of 2×10^7 protons per pulse. This attenuated proton beam then passes through the K_L target station and beam components, to be refocused and steered onto the K_S target, mounted on a movable train. The layout of the K_S beam is shown schematically in Fig. 3. The target unit including the choice of heads is similar to that for the K_L beam. Two vertical bending magnets upstream of the target are used to direct the proton beam onto the target at the same incident angle as for the K_L beam and hence produce a K_S beam with the same initial momentum spectrum.

After the target, a bending magnet serves to deflect the primary beam further downwards and to sweep charged secondaries away from the neutral beam line. These are then absorbed in a beam-dump assembly, the core of which consists of a 1.2 m long K_S collimator with tapered-bore tungsten inserts. This collimator defines the acceptance (± 0.5 mrad) of the beam emerging at a distance of 7.1 m from the target. Just downstream of the collimator is the K_S anticounter (see subsection 3.1). Both collimator and anticounter can be retracted to allow passage of the K_L beam.

Altogether the K_S beam train consists of the two vertical bending magnets, the target unit, and the beam-dump/collimator. These occupy an overall length of 14.4 m and are mounted on three chariots. This train is motorized so as to travel on precisely aligned rails over a longitudinal distance of 48 m inside the first section of the evacuated tank which encloses the kaon decay region. By stopping the train successively at each of 41 stations, spaced 1.2 m apart, K_S decays can be observed over the whole length of the K_L fiducial region. The transverse target position varies by ± 1 mm (± 0.5 mm) horizontally (vertically) over the 41 stations. The reproducibility of the target position in returning to the same station is 0.2 mm. The electric current for the magnets is picked up by contacts which slide on copper busbars mounted between the rails. All other supplies, including cooling-water hoses for the magnets, and cables for the various motors, high voltage, and signals, enter the vacuum tank midway between the two ends of the 'railway'. They are carried to the train by means of a flexible cable track which unrolls as the train moves.

Typical counting rates recorded by the detectors with the K_S beam, with the train stationed half-way along its course (station 21), are also given in Table 2. The measured kaon momentum spectrum at production is plotted in Fig. 4. This spectrum is obtained from measured $K_S \rightarrow \pi^+\pi^-$ decays with acceptance and lifetime unfolded, and its normalization corresponds to the solid angle subtended by the K_S beam.

2.3 Decay region

The kaon decay region is enclosed within a cylindrical steel vacuum tank, constructed in two sections whose inside diameters are 1.92 m and 2.40 m, respectively, covering a total length of 111 m. The K_S train and the fiducial length over which kaon decays are selected lie in the upstream section. The 400 m^3 volume of the tank is evacuated by means of trochoid and Roots pumps to a pressure of typically 3×10^{-3} Torr.

The downstream end of the vacuum tank is closed by a thin window in the form of a spherical cap, 2.4 m in diameter. The window is composed of three superimposed layers of Kevlar fibre cloth, each 250 μm thick, which were placed in a mould and impregnated with epoxy under vacuum. The thickness corresponds to 3×10^{-3} radiation lengths. It is glued onto circular metal flanges, which hold it at its outer and inner edges. At its centre the window is sealed onto a beam pipe of 164 mm inside diameter in order to allow the kaon beam to complete its path in vacuum. A prototype of the window was tested to withstand an overpressure of 3 atm.

The decay vacuum tank and exit window are followed by a further cylindrical steel tank, 2.8 m in diameter (see Fig. 1b). The beam pipe is suspended along the axis of this tank, which houses the drift chambers of the experiment and is filled with helium gas at atmospheric pressure to minimize multiple scattering. The helium purity is typically maintained at 98%. The tank is closed in front of the charged decay hodoscope by a 12 mm thick end-cap made of aluminium alloy. The helium tank serves also as a safety enclosure, capable of withstanding the depression should the thin Kevlar window rupture.

2.4 Calibration beams

Provision is made to supply beams of pions, electrons, or muons for calibration purposes. Electrons are produced by converting photons from a target station ≈ 400 m upstream of the K_L target, and negative pions are selected from this same target station from which the primary proton beam normally originates. These beams are momentum selected and are transported through the beam components to allow a complete coverage of the calorimeters by vertical sweeping of the beam and horizontal displacement of the calorimeter. To obtain muons, the normal K_L beam is stopped just after the target, and the sweeping magnets are switched off. This allows the muons from pions produced at the target and the beam dump to illuminate the detector components uniformly.

3. SCINTILLATION COUNTERS AND HODOSCOPES

Several scintillation counters are employed in the experiment. These counters serve to define the leading edge of the K_S charged and neutral decay distributions, to fix the trigger timing of the charged and neutral decay modes, and to suppress unwanted K_L decay modes. A general description of the counters is presented here, and further details regarding their use can be found in the subsequent sections.

3.1 K_S anticounter

The beginning of the K_S decay region is defined by a small scintillation counter with 7 mm of lead placed directly in front of it. This counter is situated 20 mm downstream from the K_S collimator on the K_S beam train (see Fig. 4). It vetoes upstream decays at the trigger level and thus establishes a well-defined leading edge to the decay distribution, which is used to calibrate the energy scale of the liquid-argon calorimeter (see sub-subsection 5.5.5).

3.2 Anticounter rings

Four large anticounter rings are placed in the downstream region of the vacuum tank and between the wire chambers in the helium tank (see Figs. 1a,b). These anticounters remove unwanted three-body decay modes of K_L at the trigger level by detecting photons outside the solid angle subtended by the calorimeters. These counters reduce the amount of $3\pi^0$ background in the $K_L \to 2\pi^0$ sample by a factor of 3.

Each counter consists of two planes of scintillator, read out by wavelength-shifter bars which are connected to a single photomultiplier tube. The counters are mounted with 5 cm of iron in front of the two scintillators and 2.5 cm of iron between them. There are 16 counters per ring for the two upstream rings and 8 counters per ring for the two downstream rings (Figs. 5a–c). For photons, these counters are 50% efficient at 300 MeV and $\approx$ 95% efficient above 1 GeV.

3.3 Charged-decay hodoscope

A hodoscope of scintillation counters is placed in front of the liquid-argon calorimeter to detect charged decay modes and to start the trigger system for these decays. The hodoscope consists of 18 horizontal strips and 2 vertical strips, each 2 cm thick, which cover a circular region of 1.2 m radius around the beam pipe (Fig. 6).

3.4 Neutral-decay hodoscope

In order to start the trigger system for neutral decay modes, a plane of scintillators, 12 mm thick, is installed inside the liquid-argon calorimeter after 12.5 radiation lengths*) [4]. The plane is split into six vertical strips as shown in Fig. 7. A wavelength-shifter plate, 3 mm thick, is placed behind each scintillator and transmits light to a photomultiplier tube. The photomultipliers are located at room temperature on top of the cryostat. The response of the scintillators has been measured with muons, with the counters submerged in liquid argon. The light yield is typically 40 photoelectrons at the scintillator midpoint, compared with 50 photoelectrons in air. Attenuation lengths are 2 to 3 m, comparable with the size of the counters. Thresholds are set so that the counters are $\approx$ 80% efficient for minimum-ionizing particles at the centre of each counter. Two of the counters (labelled 2L and 2R in Fig. 7) exhibit additional attenuation in their lower half owing to their shape around the hole for the beam pipe. The corresponding 100% efficiency plateau is reached for photons with an energy of 2 to 5 GeV depending on the position of impact.

3.5 Muon anticounters

Downstream of the calorimeters there are two planes of scintillator, 1 cm thick, which serve to reject muons from $K_{\mu 3}$ decays. In front of and between the two planes are 80 cm thick walls of iron absorber. The first plane has horizontal strips and the second plane has vertical ones. The strips overlap by 5 mm to ensure full efficiency over the whole area of $2.7 \times 2.7\ \mathrm{m}^2$. Photomultipliers are connected to both ends of each scintillator for readout, except for the central counters ending on the vacuum pipe which have only one photomultiplier each. The efficiency has been measured to be $> 99.5\%$.

---

*) Scintillator SCSN38 and wavelength shifter Y-7 (produced by Kyowa Gas Chemical Industry Co., Ltd., Tokyo, Japan) did not craze after submersion in liquid argon.

4. WIRE CHAMBERS

4.1 Mechanical construction

The experiment uses two drift chambers of similar construction, located 24.5 m apart and bolted to the helium tank. The first chamber is situated 100 m from the beginning of the 50 m long decay region. Each chamber consists of four wire planes. The orientation of the wires is vertical in the first plane, horizontal in the second plane, and at 53° and 143° in the third and fourth planes, respectively. The wires define two orthogonal coordinate systems, tilted by 53°. The origins of the two systems are separated (Fig. 8), so that no more than two wires cross at any one point in the projection plane perpendicular to the beam. This is the optimal choice for resolving left/right ambiguities.

These chambers are unusual in that there are no field-shaping wires in the sense-wire plane. The sense wires are of 30 μm diameter gold-plated tungsten, spaced 6 mm apart. The wires are stretched by a force of 1.3 N and soldered to printed boards on the chamber frame. The gap between the anode and cathode planes is 8 mm. The cathode planes are at high voltage and consist of 25 μm Mylar foils coated with graphite and glued to Vetronite frames. These frames are sandwiched between aluminium bars for mechanical support (Fig. 9).

A special feature of the chambers is the central hole which accommodates the evacuated beam pipe. Wires and cathode foils terminate on Vetronite rings, assembled on a thin aluminium cylinder surrounding the beam pipe. The outer diameter of the rings is 200 mm in the first chamber and 224 mm in the second chamber.

The chambers are operated at a voltage of 2.85 kV with a gas mixture of argon (70%) + isobutane (30%) bubbling through isopropanol at 3 °C. The drift velocity is 55 μm/ns for 85% of the drift space, but is lower in the middle between the wires.

4.2 Electronics

Each wire signal is amplified, shaped, and split into two separate emitter-coupled logic pulses in preamplifier boxes mounted on the chamber frames. The amplifiers [5] were taken from a previous experiment. One wire signal is connected to a set of coincidence registers, the other is used for the drift-time measurement (Fig. 10).

In the coincidence registers a hit is recorded if it occurs within 180 ns after passage of the particle as measured by the event time t_0 (trigger Level 1, sub-subsection 7.1.1). The Level 1 pretrigger signal starts encoding logic to form addresses from the contents of the hit registers. Each chamber plane has its own encoder. Adjacent wires are grouped into clusters with a maximum of five wires per cluster. Up to four cluster addresses and widths can be recorded per plane. The presence of more than four clusters is signalled by an overflow bit. The information on the number of clusters in each plane is passed on to the trigger logic for the Level 3 trigger decision. A Level 3 trigger signal initiates the transfer of the stored cluster addresses to a buffer card in the main data-acquisition FASTBUS crate.

For drift-time measurement the second amplifier outputs are connected in groups. The 432 wires in each plane are divided into six groups; every fourth wire in each group is connected to the same TDC. In this way 24 TDCs are enough to record the signals of one plane. The grouping is made in such a way that the pions from a $K \to \pi^+\pi^-$ decay should always hit different groups. The TDCs are located in the main data-acquisition FASTBUS crate. They employ 100 MHz scalers, which are started by the trigger t_0 and stopped by the wire signals. In order to reduce the error on the time measurement, the time of the start pulse is recorded in 2 ns bins.

4.3 Performance

The timing of each wire with respect to the charged decay hodoscope is adjusted using muons. The efficiency of the chambers is then determined in K_S and K_L runs, using charged decays with a reconstructed vertex. In order to reconstruct a space point, hits in at least three out of four planes are required. The frequency of missing hits in one plane determines the inefficiency. If two of the four possible hits in the same space point are missing, the event is lost. The average efficiency per plane is better than 99.3%. The estimated loss of good events due to inefficiencies or overflows is a few per mille.

The reconstruction accuracy using drift times is estimated by comparing with Monte Carlo simulation both the quality of fit in well-constrained (4-hit) space points and the distribution of the closest distance of approach of two tracks in $K_S \to \pi^+\pi^-$ decays. The average measurement error in one wire plane is around 500 μm. This is too large to resolve left/right ambiguities correctly in all cases. Wrong assignments cause tails in the distributions and lead to an r.m.s. error of about 750 μm in the measurement of either transverse coordinate. For high-energy kaon decays, the resolution in the distance of closest approach of two reconstructed tracks is 5 mm in the middle of the decay region.

From the dependence of reconstruction accuracy on momentum it is found that at 70 GeV/c kaon momentum the errors due to measurement and multiple scattering are about equal; for higher momenta the measurement error dominates. The largest single contribution to this error is the time-slewing effect in the wire signal. The longitudinal decay vertex resolution is typically 80 cm at the centre of the 50 m fiducial volume and varies by ± 40 cm over the decay region and kaon momentum spectrum. This vertex resolution is comparable to the vertex reconstruction accuracy in neutral decays.

5. LIQUID-ARGON CALORIMETER

The liquid-argon calorimeter has been designed to measure $K^0 \to 2\pi^0 \to 4\gamma$ decays and to discriminate against other K_L three-body decay modes, both charged and neutral. This requires a high level of energy and space resolution, and uniformity of response. The following subsections describe the liquid-argon calorimeter hardware, readout electronics, and performance. The principal design parameters and performance figures are listed in Table 3. For more extensive discussions of the hardware design and assembly, or of the electronics design, see refs. [6].

5.1 Hardware description

5.1.1 Basic layout

The liquid-argon calorimeter consists of a stack of lead conversion plates, which are aluminium clad, alternating with printed-circuit board readout planes. As shown in Fig. 11, the calorimeter is physically divided into left and right halves. The plates, weighing $\approx$ 9 t in total, are supported by stainless-steel rods and suspended from the cryostat cover plate. The useful surface of the calorimeter is limited to an octagon with an inscribed radius of 1150 mm. Most of the tie rods traversing the calorimeter, and which are needed to maintain stack spacing, are located outside this fiducial region. The calorimeter was designed to allow an evacuated beam pipe, transporting the neutral beam, to pass through its centre.

Figure 12 shows the cell structure, consisting of the aluminium-clad sandwich plate, two liquid-argon gaps, and a double-sided strip readout plane. The length of one cell is 7.3 mm or 0.31 radiation lengths. The uniformity of the cell size is maintained between the rigid conversion plates by G-10 spacers, which pass through the readout plates and are held in place by the tie rods. Plastic spacers, distributed over each readout plane, keep the readout planes centred in the liquid-argon gaps. The readout planes are fixed relative to the conversion plates by only the two central tie rods in order to allow for differential shrinkage. Planes with vertical and horizontal strips alternate for a total of 80 cells. The scintillator plane forming the neutral decay hodoscope (see subsection 3.4) is placed midway, dividing the calorimeter into front and back halves, each with 12.5 radiation lengths.

The readout strips are discontinuous at the vertical and horizontal midplanes, so that sets of horizontal and vertical strips form quadrants. The strip pitch is 12.5 mm and there are 96 horizontal and 96 vertical strips per quadrant. The strips are connected longitudinally, but the readout of the front and back halves is separate. In total there are 1536 channels.

5.1.2 Channel connection to preamplifiers

Each calorimeter channel consists of 20 longitudinally connected horizontal or vertical strips. During operation the strips are at high voltage (2 kV) and the plates are at ground. The calorimeter capacity to ground is ≈ 5 nF and there is ≈ 0.6 nF cross-talk capacity between two neighbouring channels. The preamplifiers are located on top of the cryostat at room temperature.

To avoid the complete loss of a readout channel when a single strip becomes shorted to ground (see subsection 5.3), the 20 strips of a channel are subdivided into 2 interleaved groups of 10 strips. Each group is brought out of the cryostat separately and then connected externally to form a complete channel. In the event of a short circuit, this connection may be removed, allowing the continued use of the half-channel but at the expense of reducing the shower sampling to half.

A section through the 16-conductor low-impedance flat cable (connecting to eight calorimeter channels) is shown in Fig. 13. The 4.5 m long cable is made of copper strips embedded in Kapton insulation. Each cable conductor has a total capacity of ≈ 2.5 nF and an inductance of 360 nH, and sustains at least 3 kV with respect to the neighbouring conductors and to ground.

5.1.3 Channel calibration systems

Electronic signals simulating calorimeter pulses are injected at three separate points in the readout chain. Two injection points outside the cryostat are run as a separate system and are discussed in sub-subsection 5.4.1. Inside the cryostat, a charge is injected into each channel via capacitors made from double-layered, copper-plated G-10 strips. Signals are multiplexed to pulse one in four channels at a time. This system is used to measure and monitor electronic gains and non-linearities as well as the channel-to-channel cross-talk. The calibration capacitors are measured individually with an accuracy of 0.1%.

5.2 Cryogenic system

5.2.1 Cryostat

The cryostat, an expanded view of which is shown in Fig. 14, is composed of an inner (liquid-argon) vessel, an outer (vacuum) vessel, front and back beam windows, a cover plate, and two concentric central tubes. The inner stainless-steel vessel is sealed to the outer one by means of an O-ring, and one of the central tubes is welded in place after insertion of the calorimeter to complete the inner vessel. The warm cover plate, which supports the calorimeter, seals the liquid-argon vessel without any vacuum insulation. The necessary feedthroughs for signals, argon transfer, cooling, etc., pass through the cover plate.

Beam windows of aluminium close the front and back of the vacuum vessel. The outward pressures on the liquid-argon vessel are transferred to the beam windows by means of truncated G-10 cones. The central beam pipe passes through and is sealed by the beam windows. There are 0.90 (0.17) radiation (interaction) lengths of material upstream of the first liquid-argon gap, and a corresponding 1.34 (0.25) radiation (interaction) lengths of material downstream from the last calorimeter cell.

5.2.2 Cooling systems

Two independent (normal and back-up) cooling systems maintain a stable liquid-argon temperature (Fig. 15). In the normal system, argon gas is recondensed by means of a heat exchanger filled with liquid nitrogen and located outside the cryostat. The liquid nitrogen is kept at 2.3 bar (85 K) by two Philips single-cylinder cryogenerators. The reliquefied argon flows through an oxygen absorber when returning to the cryostat. This system is self-regulating and maintains a constant 1.2 bar absolute cryostat pressure.

When the normal system is not running, for instance during a power cut, the back-up system recondenses the argon using liquid nitrogen stored in a pressurized dewar near the cryostat. The liquid nitrogen flows through a heat exchanger within the cryostat, venting to the outside. This system functions with minimal power requirements, depending only on the nitrogen being replenished.

The thermal loss of the cryostat is about 1500 W, divided into: 50% due to solid conduction, 25% due to radiation, and 25% due to other sources such as convection, transfer losses, etc.

5.3 Operational experience

The liquid-argon calorimeter was cooled down twice for data-taking, for periods of about four and five months, respectively. In this subsection we discuss two operational problems: shorted calorimeter channels and loss of signal in the liquid argon.

During the first cool-down, short circuits between the readout strips and conversion plates developed in two regions. These channels were completely eliminated from the readout. In response, the cable design described in sub-subsection 5.1.2 was implemented. During the next running period, the number of shorted regions increased at cool-down and with each argon fill (see below) to eight regions affecting 6% of the readout channels. None of these regions overlapped so that signals were read out from all calorimeter channels. The adverse effects of the shorted regions on the uniformity of response or resolution were found to be minimal. A full understanding of the origin of the short circuits has not been possible since they disappear at room temperature, and a dismantling of the calorimeter has not been permitted in the time allowed by the experimental programme.

During the two run-periods, the energy response of the liquid-argon calorimeter decreased with time at a rate varying between 0.03% and 0.5% per day, depending on the fill. The argon was replaced several times to maintain sufficient signal. One fill was found to be contaminated from the start and was immediately replaced. These overall rates and changes in rates of signal loss have not been understood. The phenomena, however, cannot be explained either by oxygen contamination — which was continuously monitored to be $\approx$ 1 ppm or less — or by the outgassing of materials in the cryostat.

5.4 Calorimeter readout electronics

5.4.1 Input circuit

In a configuration with a high channel capacitance (5 nF + cable) and a 4.5 m long cable to the preamplifier, the damping of the input circuit is critical, especially when a fast response is needed [7]. The solution adopted, which also allows good cross-talk rejection, is to use low-impedance flat cables and a transformer with an optimum turns ratio of 14, i.e. at the noise minimum. These characteristics require proper damping to be achieved with a 3.3 Ω resistor in the input circuit. This resistor is submerged in the liquid argon and has the equivalent noise of a 1 Ω room-temperature resistor.

Calorimeter signals are shaped by a 1.6 μs differentiation in order to avoid overlapping signals, followed by two stages of 50 ns low-pass filtering. The circuit diagram and the computed direct and cross-talk signals are given in Figs. 16a,b for two values of damping resistance R_S. Note that the damping is more critical for the cross-talk signal, which is sensitive to two coupled ringing circuits. The cross-talk signal is reduced both by the size of the cross-talk capacitance (0.6 nF) and by the differentiation time constant (30 ns) of the coupling. This reduction is further improved by the choice of sampling time in the sample-and-hold measurement.

There are two preamplifier outputs: one goes to the sample-and-hold signal measurement; the other is used in a double differentiated sum for a fast-trigger energy measurement. Also, there are two 50 pF (± 1%) glass calibration capacitors on either side of the 100 nF blocking capacitors, upstream of the transformers. These are used for on-line calibration and hardware debugging.

5.4.2 Sample-and-hold signal measurement

With a transformer at the input of the preamplifier, low-frequency noise is dominant and can be effectively eliminated with double differentiation. This is achieved by sampling the input signal at three different times, using CMOS switches, and forming the sum (see Fig. 17a)

$$Q_{out} = (Q_B - Q_A) - (Q_C - Q_B)\,,$$

where Q_{out} is the total measured charge, and Q_A, Q_B, and Q_C are the charge samples.

With the time between successive samplings (700 ns) being larger than the signal rise-time (400 ns), the dependence on exact timing is not critical and the cross-talk rejection is efficient and stable. The 1.6 μs decay-time constant of the preamplifier is compensated by a slightly modified weighting of the charges Q_A, Q_B, and Q_C.

Two sample-and-hold outputs exist (see Fig. 17b): one to the ADCs and the other to the trigger for photon counting (see sub-subsection 7.1.3). For an event accepted by the trigger, the switch S_{II} is opened to isolate the total measured charge stored on capacitor C_{II} which is ready to be digitized. The upstream switches are then closed to clear the charges stored on C_A, C_B, and C_C, and the sample-and-hold is ready for a new event.

5.4.3 ADC system

FASTBUS ADC modules, of 96 channels each, are used to digitize the sample-and-hold measurements [8]. Each module has six 12-bit ADC chips*) which take 2 μs for conversion. In order to minimize queuing time, neighbouring channels are fed to different ADCs. Including multiplexing and storage, the total conversion time is 4 μs per channel, typically 15 μs for a good event. The typical sensitivity is 9 MeV per least count with a dispersion of ± 10% over all 1536 channels.

Both the total conversion time and the amount of data recorded are reduced using a zero suppression scheme. Working at the analog level, only those channels above a certain threshold (typically 150 MeV per channel) and their neighbours (three on either side) are converted. Also, the channels in the front and back halves are correlated so that the corresponding channels are always converted.

5.5 Performance of the liquid-argon calorimeter

5.5.1 Electronic calibration

To measure pedestals and electronic channel gain, two kinds of events are recorded: i) using a random clock trigger and ii) with a fixed amount of charge injected into every fourth calorimeter channel. For these events, all 1536 channels are digitized and recorded. They are taken both during the beam spill, at a frequency proportional to beam intensity, and out of the spill. From the random events, the r.m.s. of the pedestals gives 16 MeV per channel in electronic noise. The coherent part of the noise is found not to be significant. Over the long term (period of days), pedestals exhibit a small random variation below a 10 MeV level.

---

*) DATEL INTERSIL 827 MC.

Using events with charge injected in every fourth strip, the absolute value of channel-to-channel cross-talk is measured to be less than 1.0%. The electronic channel gains, also obtained from these events, exhibit a small overall drift correlated with the temperature in the experimental hall. Typically, there is a daily periodic shift of less than 0.8% peak-to-peak and an overall 1% drift during a five-month run period. This gain/temperature correlation is measured to be 0.15%/°C. For data analysis, individual electronic channel gains are calculated from long-term (≈ 24 hours) averages, and each channel gain is corrected hourly by the measured overall temperature drift of the 1536 electronic channels.

Finally, electronic calibrations taken in and out of the beam spill agree to better than 2×10^{-4}, showing no significant rate dependence.

5.5.2 *Energy resolution*

The calorimeter energy resolution can be divided into three terms: i) shower fluctuations, ii) uniformity of response across the calorimeter, iii) electronic noise. To obtain the shower fluctuation component, electron beams of energy 12, 15, 20, 35, 50, 80, 100, and 120 GeV were used (see Fig. 18 for the 15 GeV and 80 GeV energy distributions). A Gaussian distribution has been fitted to the measured energy deposition. The energy spread of the beam can be neglected if the fit is not extended too far to lower energy, where bremsstrahlung of electrons broadens the peak. An energy resolution of $7.5\%/\sqrt{E}$ (E in GeV) is obtained at all but the lowest electron energy, where electronic noise begins to contribute (see Fig. 19).

To obtain the uniformity of response, a scan over all the calorimeter strips in the fiducial volume was done with electrons of 80 GeV. The response was found to be independent of the impact position on the calorimeter to within ±0.5%.

At low energy the electronic noise of 16 MeV per channel contributes to the energy resolution. It has been verified that the electronic noise of different channels is uncorrelated. Thus for electromagnetic showers of several GeV, the noise contribution is 16 MeV times $\sqrt{N}$, where N is the number of channels used to sum up the energy in the shower. Typically, N is 40 for low-energy showers, giving about 100 MeV of noise.

Combining these three contributions, we get the following expression for the energy resolution (E in GeV):

$$\frac{\sigma_E}{E} = \left[\left(\frac{0.1}{E}\right)^2 + \left(\frac{0.075}{\sqrt{E}}\right)^2 + (0.005)^2\right]^{1/2} .$$

5.5.3 *Spatial resolution*

The spatial resolution of the calorimeter is obtained by comparing the reconstructed shower position with the electron track impact point extrapolated from the wire chambers. A Gaussian fit to the difference, as shown in Fig. 20, has a standard deviation of 0.75 mm. This value includes chamber resolution and multiple scattering and can thus be considered as an upper limit to the spatial resolution for photons.

5.5.4 *The π^0 mass resolution and the background rejection*

Good energy and good space resolution of the liquid-argon calorimeter are important in order to minimize the amount of $K_L \to 3\pi^0$ background in the final $2\pi^0$ sample. The $3\pi^0$ decay mode, which is 200 times more abundant than the $2\pi^0$ mode, is partly reduced by an extra photon detected in either the calorimeter or anticounter rings. The removal of the remaining background depends on the π^0 mass resolution in the following reconstruction method.

Using the kaon mass constraint, the longitudinal kaon vertex position z_v in four-photon events is calculated, in the small-angle approximation:

$$z_v = \frac{1}{m_K} \left\{ \sum_{i,j<i} E_i E_j \left[(x_i - x_j)^2 + (y_i - y_j)^2 \right] \right\}^{1/2} ,$$

where E_i, x_i, and y_i are the photon energy measurements and transverse positions.

Since the $3\pi^0$ events have two photons missing, their reconstructed vertex appears closer to the calorimeter. Thus a large part of this background can be eliminated with a fiducial cut. (This is also done on-line, see subsection 7.3.) To remove the remaining background, the value of z_v is used to calculate the two-photon invariant mass for the three combinations:

$$m_{ij} = \frac{1}{z_v} \left\{ E_i E_j \left[(x_i - x_j)^2 + (y_i - y_j)^2 \right] \right\}^{1/2} .$$

Choosing the best mass combination, a cut is applied around the π^0 mass in the two-dimensional mass plot for the two π^0's. From Monte Carlo simulation it is seen that the residual $3\pi^0$ background uniformly populates this plot, so that the amount of $3\pi^0$ background under the $2\pi^0$ mass peak varies as $\sigma^2_{m_{\pi^0}}$. With increasing energy the spatial resolution becomes a contributing factor in the mass resolution. However, with a spatial resolution of better than 1 mm, the energy resolution dominates the mass resolution up to above 200 GeV kaon momentum. Other contributions to the $\sigma_{m_{\pi^0}}$ are due to reconstruction effects of overlapping photons and of photons falling on quadrant boundaries. This worsens the resolution by ≈ 20%.

Figure 21 shows the π^0 mass distribution for $K_S \to \pi^0\pi^0$ decays. The resolution is about 2 MeV. The $3\pi^0$ background under the mass peak in K_L decays varies from ≈ 0.1% to ≈ 10% moving towards the calorimeter through the 50 m decay region.

5.5.5 *Energy scale and linearity*

The absolute energy scale of the liquid-argon calorimeter is established to 0.1% using the K_S anticounter. Initially, the calibration is set to a few per cent by an 80 GeV/c electron beam. Corrections to the photon energy are applied in off-line reconstruction for electronic non-linearity and for small amounts of energy (≈ 1%) in shower tails not read out by the on-line zero suppression scheme. The final energy scale is then obtained by requiring the leading edge of the measured $K_S \to \pi^0\pi^0$ vertex distribution to coincide with the known anticounter position. As can be seen from the equations in the previous sub-subsection, the overall calibration factor is equivalent to a change in the length scale. For a distance of 100 m from the centre of the decay region to the liquid-argon calorimeter, a 0.1% energy calibration is equivalent to fixing the length scale to 10 cm, corresponding to 10% of the vertex resolution. Typically, the experiment runs for 10 out of every 48 hours in the K_S beam mode. Within this period enough statistics are accumulated for an energy scale determination to the 0.1% level at each of ten different positions of the K_S beam train. Figure 22 presents the vertex distribution for $K_S \to \pi^0\pi^0$ with a Gaussian-smeared K_S decay curve superimposed. The collimator position uncertainty which results from this fit is 8 cm. The vertex position resolution is 120 cm at the centre of the fiducial region and scales relative to the distance from the calorimeter.

The linearity of the calorimeter has been checked with electron beams in the range 12 to 120 GeV. The response is linear to within a systematic uncertainty ≈ 0.3%. In addition, for low-energy photons in the range 5 to 15 GeV, the linearity is better than 1%. This can be seen from two independent methods: i) using the combined mass constraints of the two π^0's and the kaon in $2\pi^0$ events, ii) using the m_{π^0} mass constraint in combination with the reconstructed charged track vertex in $\pi^+\pi^-\pi^0$ decays. Since the kaon momentum is derived from four photons, the non-linearity over the kaon momentum spectrum is much below the percent level.

The overall calibration is monitored throughout a run-period lasting several months. Typically, the beam is switched from K_L to K_S running conditions every two days, which is sufficient to determine reliably the slow overall shifts of the energy scale.

5.5.6 The 'e/μ' ratio

It is well known that the processes contributing to the energy losses for e,γ and minimum-ionizing particles depend in a different way on the Z of the material. In the present configuration, the liquid argon contributes 10% to the radiation length and 25% to the mean minimum-ionization loss. Since it is the ionization loss of the shower components that is detected in the argon, one might naïvely expect that the signal seen should correspond to 25% of the shower energy. However, from the electromagnetic gamma shower Monte Carlo simulation (EGS3 [9]), only 17.5% of the energy loss for e,γ is expected to occur in the liquid argon. This relative calorimetric response between electromagnetic showers and minimum-ionizing particles is frequently expressed in terms of an 'e/μ' ratio of (17.5/25 =) 0.7 in this case.

From a sample of pions taken with a pion calibration beam, the minimum-ionizing energy loss can be extracted from those pions which do not interact in the front of the liquid-argon calorimeter. From a Gaussian fit to the pion minimum-ionizing peak, a mean of 207 ± 1 MeV is obtained, measured in terms of the calibration fixed for e,γ. A calculated mean minimum-ionization loss of 136 MeV is expected for the front of this calorimeter. Thus the 'e/μ' ratio is 136 MeV/207 MeV = 0.66, in good agreement with the ratio expected from the EGS studies and the mean ionization energy loss.

6. HADRON CALORIMETER

6.1 Description of the detector

The hadron calorimeter (Fig. 23) consists of an iron/scintillator sandwich of 1.2 m total iron thickness (6.7 nuclear absorption lengths). It is divided longitudinally into two separate modules, each consisting of 24 steel plates, 25 mm thick, of dimensions $2.7 \times 2.7\ \mathrm{m}^2$.

Each scintillator plane*), inserted between the steel plates, consists of 44 separate strips of dimensions 1.3 m × 11.9 cm × 4.5 mm. There are 24 (25) scintillator planes in the front (back) module. In consecutive planes the strips are alternately aligned horizontally and vertically. Since each strip spans only half the calorimeter, the scintillator planes form a quadrant structure similar to that of the liquid-argon calorimeter. In each module the corresponding horizontal or vertical strips are coupled to a 3-inch phototube**) by Plexiglas light-guides. Before assembly, all scintillators coupled to a common tube were selected for equal light attenuation, and the effective transmission of their light-guides was balanced to ensure a homogeneous response. Since the energy deposition enters into the trigger conditions, all phototubes are adjusted to give the same response for muons to within 10%.

6.2 Laser calibration

The hadron calorimeter possesses 176 readout channels. The analog signals are fed into linear mixers which match the impedance to twisted-pair output and allow for an optional amplification of about 25 for the measurement of minimum-ionizing muons as well as for the input of electronic test pulses. Subsequent integrators split each signal into two parts. The first part is an integrated

---

*) The material used is BIS-MSB in a Plexiglas base.

**) SLC L75 B07.

phototube signal which simulates the slower signal of the liquid-argon calorimeter and is used for energy measurement in the same sample-and-hold/ADC system. The second part forms a fast analog sum which is used as an energy measurement in the trigger.

A laser calibration system (Fig. 24) has been installed to monitor the performance of the complete readout chain. A beam of ultraviolet light (337 nm, 10 ns pulse width) from a nitrogen laser is enlarged by a lens system and converted into blue light (420 nm) in a scintillator sheet. The blue light is distributed to an array of quartz fibres (200 μm diameter, 8 m long) and transported to each light-guide. A set of grey filters allows the light intensity to be varied, under computer control, over a dynamic range of 1:140 in order to calibrate the characteristics of each readout channel. The intensity of the laser is measured on a 'reference tube' and compared with the β^+ spectrum of a ^{22}Na source embedded in a NaI crystal. The average laser pulse height in units of the fitted β^+ annihilation peak position is thus independent of the gain of the reference tube. In addition, the intensity of single laser pulses is measured with a photodiode. The laser runs continuously so that a few pulses are recorded per beam spill.

6.3 Hadronic energy reconstruction

A large fraction of pions deposit a significant amount of energy in the 1.3 absorption lengths of the liquid-argon calorimeter. Thus the calorimetric response to hadronic showers is calibrated with the combined system. As described above for the liquid-argon calorimeter, the relative calibration between individual channels is done separately for the two calorimeters.

Pedestals are calculated from random triggers recorded during data-taking, and these are subtracted off-line from the ADC data. Special runs with muons are used to establish all relative sensitivities and the light attenuation along the scintillator strips. The typical attenuation over the full length of a scintillator is 15%. The average muon pulse height is typically 40 photoelectrons in one channel and this is used as the basic energy unit. These muon calibrations are performed about every two weeks. Short-term variations of the effective gains are monitored with the laser system. A day/night variation of about ±2% is observed, which is correlated with the temperature in the experimental hall. The average sensitivity is stable to 5%.

The average energy-sharing of hadronic showers corresponds to about 35% in the liquid-argon calorimeter and 65% in the hadron calorimeter. The hadronic response of the combined system is calibrated using pions of 12–120 GeV. The following algorithm is applied in order to optimize the energy resolution:

i) Relative energy units are transformed into GeV. For the hadron calorimeter, a scale factor of 0.72 GeV per average muon pulse height has been determined from pions having no interaction in the liquid-argon calorimeter. For the liquid-argon calorimeter, an overall factor of 1.3 adjusts the recorded energy of pions to the response for electrons of the same energy.

ii) Overlapping showers are disentangled assuming an exponential lateral shower profile and using the energy distribution in the projection without overlap.

iii) To equalize the different responses for hadronic and electromagnetic shower components, a lateral shape-correction weight is applied to each channel content; this is done separately for the liquid-argon calorimeter and for the hadron calorimeter. The weights are parametrized as a third-order polynomial function of the distance between the impact point and the centre of each channel. These weights range between 0.75 for the central strip and 2.5 for strips more than 40 cm distant from the axis.

iv) A longitudinal energy correction is applied with an energy-dependent second-order polynomial F(E,R), where R is the ratio of the energy deposition in the liquid-argon calorimeter to that in the hadron calorimeter. This function corrects for the different e/π energy dependence in lead and iron, and also corrects for non-linearities in the weighting procedures. The correction varies between 1.14 at 10 GeV, with all energy in the liquid-argon calorimeter, and 0.76 at 120 GeV. The corrected response for pion showers is shown in Fig. 25.

This algorithm results in an energy resolution $\sigma_E = 0.65/\sqrt{E}$ for E above 12 GeV (see Fig. 26). The improvement of the weighting algorithm can be seen by comparison with the unweighted energy resolution of $1.20/\sqrt{E}$.

7. TRIGGER SYSTEM

The trigger system has been designed to select $\pi^+\pi^-$ (charged) and $2\pi^0$ (neutral) decays in a K_L or K_S beam. Since these channels are rare decays in the K_L beam, the trigger must have good discrimination against common three-body decays and be able to operate with a high beam intensity to permit accumulation of the desired statistics.

Charged and neutral two-pion decay modes are processed simultaneously and trigger conditions remain unchanged when switching from the K_L to the K_S beam. Each event is classified as a charged or neutral trigger — or both — according to trigger conditions. The trigger logic is implemented using programmable units [10] to allow flexibility for incorporating different selection criteria. The logic inside these electronics units is loaded by the on-line computer with a compiled set of logic input files. The trigger system is logically separated into a synchronous front end and an asynchronous second part, and is followed by a 168E dual processor system. Each stage processes and filters events independently, allowing multiple events to be handled by the system. Double buffers are employed to reduce dead-time. The memory-time of the experiment, given by the measurement of the liquid-argon calorimeter signals, is 2.1 μs.

Because of this memory-time, good $K \rightarrow 2\pi$ decays can be contaminated by overlay with other decays or other uncorrelated background particles. In order to monitor and identify this spurious overlap, two 48-channel logical-state analysers are employed. For each event, these modules record the signals from all scintillation counters and various synchronous trigger elements in a 3.2 μs window.

7.1 Synchronous part of the trigger system

The synchronous part of the trigger system makes decisions in three sequential stages. First, the information from scintillation counters is used for initial timing and fast vetoing. Next, the energy deposition in the calorimeters is used. Finally, the number of hits in the wire chambers and the number of energy clusters in the liquid-argon calorimeter are used.

7.1.1 Level 1: Scintillation counters and event time t_0

At this level, a pretrigger is generated by the combination of a cross-coincidence in either of the two scintillation counter hodoscopes and no signal from any of the scintillator veto counters. The explicit conditions for cross-coincidence in the charged and neutral decay hodoscopes are given in Figs. 6 and 7. The event time t_0 is defined by an OR of the coincidence signals from the charged and neutral decay hodoscopes. The t_0 is given by the charged decay hodoscope when a signal from both hodoscopes is present. Events with neither a signal in an anticounter ring nor a coincidence of the two muon planes generate a pretrigger. The pretrigger strobes the subsequent electronics, generates a 200 ns gate for the wire chambers, starts the TDCs, and blocks subsequent events.

Pretriggers are also generated for calibration events. Moreover, all the trigger conditions described below are released for a fraction of events giving rise to down-scaled triggers. After the initial veto of the anticounters, these special events are passed through the rest of the trigger with all subsequent conditions recorded but not applied.

7.1.2 Level 2: Fast energy measurement and K_{e3} rejection

At the second level of the synchronous trigger, fast analog sums of the energy deposition in the calorimeters are used. These energy sums are made for each quadrant of the four longitudinal sections of the liquid-argon calorimeter, and hadron calorimeter and are available about 250 ns after t_0.

Charged decays have to satisfy a minimum total energy threshold (from both calorimeters). Neutral triggers must pass both a minimum energy threshold in the liquid-argon calorimeter and a maximum threshold in the hadron calorimeter. This maximum hadron energy threshold condition, which is not applied until Level 3, is softened by forming the OR with the condition that there are not two charged tracks in the first wire chamber (in practice, less than eight wires hit).

The K_{e3} decays produce an electron and a pion in the detector. Electrons can be identified by their early shower development in the liquid-argon calorimeter and with little or no energy in the hadron calorimeter. An initial rejection of these three-body decays is done by requiring that no track should deposit more than 4/5 of its energy in the front part of the liquid-argon calorimeter. Since there is a pion as well as an electron, calorimeter energy ratios are calculated in four half-planes in order to distinguish between the two tracks and remove quadrant edge effects. The energy conditions are imposed about 400 ns after t_0. This rejects about 75% of K_{e3} events in the K_L beam, and there is a corresponding 2% loss of $\pi^+\pi^-$ events as measured in the K_S beam.

If the energy requirements are satisfied, a general trigger is generated about 400 ns after t_0. The general trigger starts the sample-and-hold measurement of the calorimeter energy and the encoders of the wire chambers.

7.1.3 Level 3: Wire chambers and photon counting

After passing the Level 2 trigger, conditions are imposed on the number of wire chamber hits and on the recorded liquid-argon calorimeter shower peaks. For $K \rightarrow \pi^+\pi^-$ events, at least two hits are required in at least two planes of the first chamber. For neutral event candidates, the energy clusters in the front part of the liquid-argon calorimeter are counted. A set of analog comparators uses the second outputs of the sample-and-hold cards to count the number of photon showers in the horizontal and vertical projections of the front part of the liquid-argon calorimeter. An energy cluster is counted when the energy in one strip exceeds $\approx$ 1 GeV and is greater than the energy in both neighbouring strips. The $K_L \rightarrow 3\pi^0$ events are rejected by requiring that neither projection has more than four clusters. The cluster positions are also converted to a bit pattern which is read out and later used by the 168E system to reject $K_L \rightarrow \pi^+\pi^-\pi^0$ events.

If the conditions of Level 3 are satisfied, the asynchronous part of the trigger begins to process the event. The front end of the trigger remains blocked until transfer to the intermediate buffer stage is complete.

7.2 Asynchronous part of the trigger system

The asynchronous part of the trigger is composed of two parallel data streams. In the first stream the calorimeter signals are encoded (see subsection 5.4) and the digitized data are transferred to both the Arithmetic FASTBUS Interface (AFBI) and to one of two intermediate memories. The second data stream involves the transfer, by various FASTBUS modules, of digital information latched at their front end to their respective intermediate buffers. The AFBI, described below, places further cuts on calorimeter information and can remove events from the two parallel streams.

As soon as the sample-and-hold units have measured the calorimetric signals (and opened switch S_{II} of Fig. 17b), and the FASTBUS modules have transferred their data to the intermediate buffers, the front end of the trigger is re-enabled.

The calorimetric digitization stream is the slower stream and thus has two memories to help reduce dead-time. With high K_L beam intensity, the waiting time is reduced by overlapping the readout time of one event with the time needed for processing the calorimetric information of a second event into the other memory. Finally, if events are passed by the AFBI, they are read from the intermediate buffers into the memory of the first available 168E processor.

7.3 Arithmetic FASTBUS Interface (AFBI)

The AFBI is used to reject background three-body decays based on the more accurate digitized calorimetric energy measurements. While the calorimeter channel information is being digitized and stored in memory, a pedestal-subtracted, gain-corrected set of channel energy measurements is sent to the AFBI. In parallel with a cycle time of ≈ 150 ns, the AFBI calculates energy sums and the first and second moments: ΣE_i, $\Sigma x_i E_i$, and $\Sigma x_i^2 E_i$, where the sums are over calorimeter channels. These quantities are then used to place the following cuts on events:

i) Charged events:
  a) minimum threshold for the sum of the energy in both calorimeters;
  b) minimum threshold for the energy in the hadron calorimeter;
  c) limit on longitudinal shower development for electron rejection (in four half-planes of the calorimeters, see sub-subsection 7.1.2).

ii) Neutral events:
  a) minimum threshold for the energy in the liquid-argon calorimeter;
  b) centre of gravity of the energy deposition, from the first moment;
  c) longitudinal vertex position, derived from the energy sums and second moments. (See sub-subsection 5.5.4 for a discussion of this cut.)

Both sets of quantities are calculated for all events, but the rejection is applied according to the event type. The sums and calculated cut values are included in the event readout. For checking purposes, a fraction of the events have the calculations performed with the rejection inhibited.

The AFBI performance has been measured with down-scaled events. Table 4 presents the rejection factors for those events which reach the AFBI. About 15% of the events entering the AFBI are labelled as both charged and neutral and consequently have no rejection applied. For K_L, the AFBI reduces by a factor of 5 the number of events with only a neutral trigger, and by a factor of 2.5 those events with only a charged trigger. The overall rejection relative to events entering the AFBI is 50% for K_L and 30% for K_S. The loss of good two-pion events is below the 0.1% level.

7.4 On-line filtering with the 168E system

Before readout to tape, the final data reduction is achieved by the 168E system. Charged triggers which originate from three-body decays or from two-body decays outside the fiducial volume can be rejected by using the wire chamber and the photon-counting information.

Three-body decays are recognizable from the acoplanarity of the K^0 direction and the two charged decay tracks. For filtering purposes, this acoplanarity is measured by the distance d between the centre of the beam and the line joining the two charged impact points in the second wire chamber. Events with $d > 11$ cm are rejected. Energy clusters found by the trigger (see sub-subsection 7.1.3) are used to reject $K_L \rightarrow \pi^+\pi^-\pi^0$ events which have a photon more than 15 cm in either projection from a charged track in the liquid-argon calorimeter. For the remaining events with two charged tracks, the longitudinal position of the decay vertex is reconstructed and used to calculate the opening angle between the outgoing charged tracks. The vertex position and the kaon energy, calculated from the opening angle assuming a symmetric decay, are used to reject events outside the fiducial volume or with too low an energy.

In K_L the filter accepts 50% of charged events, including the 15% which are too complicated to be fully analysed on line and 10% which are down-scaled. The filter algorithm, implemented in FORTRAN IV and optimized for fast performance, averages 1 ms per event.

8. DATA-ACQUISITION SYSTEM

The data-acquisition system is controlled from a VAX 11/750 computer. The data associated with each event are read, via a FASTBUS system, into the dual IBM 168 emulator array [11], where they are filtered as described above. Accepted events are passed into a buffer memory which is subsequently read out into the VAX and then onto tape. The complete system is shown in Fig. 27.

8.1 FASTBUS system

The FASTBUS system [12] consists of three crates. The functions and contents of these are as follows.

8.1.1 The calorimeter ADC crate

The ADC FASTBUS crate contains 18 ADC modules (see subsection 5.4), a fast sequencer, and a buffer module. The sequencer controls the actions of the other modules in this crate. The buffer module performs three functions: it stores the ADC information in one of two buffer memories; it converts ADC data to energy and transfers these to the AFBI; and it transfers the unconverted ADC data and AFBI results, via a 32-bit bus, to a link module in the main FASTBUS crate.

The fast sequencer is externally controlled by a PDP 11/23 +, via a CAMAC interface. Outside the beam burst, the sequencer acts as a spy, so that calibration events can be read out and the ADC system be monitored by the PDP.

The final ADC data are available in the form of one variable-length memory block. The length of the data depends on the event type and is, on the average, between 200 and 300 32-bit words.

8.1.2 The main data-acquisition module crate

The data from the various detector components which are presented at the intermediate buffer level for FASTBUS readout comprise the following: three modules, each containing 192 bits of information on the state of the trigger and detectors; six TDC modules containing a total of 42 data words; a wire chamber address card containing the compacted cluster information (about 15 words); one link module to the ADC crate; two logical state analysers, each of which records the state before and after the event trigger of up to 48 detector signal lines (about 40 words each); and a scaler giving the values of several counters. The ADC data are not physically resident in this crate, but at the level of a FASTBUS readout it appears as if they are. The link module transfers the data, word by word, at read time from the ADC crate, using a private (non-FASTBUS) cable link.

8.1.3 The auxiliary data-acquisition crate

This third crate contains the main readout module, the Block Mover [13]. This module has two FASTBUS ports, and during an event readout it is master on both. It synchronously reads data from one port and writes out to the 168E array on the other, using a one-word pipeline register. Access to the main crate is via a standard FASTBUS cable/segment interconnect link. Access to the 168E array is via the auxiliary crate back-plane, followed by a cable/segment interconnect link to a specially designed module which interfaces between the FASTBUS cable at its input and the 168E memory bus.

Also resident in the main crate is a direct VAX/CAMAC interface module, the CFI [14]. This fulfils two purposes: i) it allows VAX control of the system for initialization and testing, and ii) it reads out events directly in case of a failure of the main data-acquisition path. The CFI is, however, slow and results in a data-taking rate that is reduced by a factor of 2, and moreover, it excludes on-line 168E filtering.

8.2 IBM 168 emulator system

The 168E system [15] consists of the FASTBUS-to-memory interface module, two 168E processors each equipped with data and program memories, a supervisor module based on a Motorola 68000 microprocessor, and a 3 Mbyte buffer memory (Fig. 28). The supervisor performs all controls of the 168E processors and the function of VAX interface. The connection to the VAX, which is via CAMAC, consists of a control channel (based upon the CFI control hardware) and a DMA link for transfer of the data from the buffer.

Events are directed from FASTBUS to the memory of whichever processor is available. The filter program is then initiated. If an event is rejected, the processor immediately becomes available for another event. If an event is accepted, then the data are transferred to the buffer memory under supervisor control. The events are concatenated in the buffer memory to form superevents of a length not exceeding 64 kbytes. This takes maximal advantage of the DMA speed when transferring data to the VAX.

8.3 VAX system

The VAX 11/750 computer runs VMS version 4 and is configured with 8 Mbytes of memory and 250 Mbytes of disk storage. Access to all instrumentation is via CAMAC. The maximum capacity of the CAMAC DMA link to the 168E system is 1.1 Mbyte/s. Two high-speed (75 ips), high-density (6250 bpi) STC tape drives are connected for data output. In addition, two low-density drives are connected as back-up units.

8.4 Data-taking sequence

During each active beam burst of 2.8 s duration, all the data associated with each fully triggered event are read via FASTBUS into a free 168E memory without any VAX intervention. Events are typically 400 to 500 32-bit words in length, and about 1500 events per burst are passed to the 168Es. It takes typically 0.15 ms to read each event. After filtering, about 1000 events per burst remain which are stored in the buffer memory. The mean time to filter and to transfer is about 1.5 ms.

During the 11.6 s period outside the beam burst, the buffer memory is read into the VAX memory. During a short calibration gate before each burst, a small amount of data are read directly by the VAX through the CFI, together with about 30 bytes of direct CAMAC data.

The data are reformatted and written to tape in an IBM-type format which requires half-word swapping. This task takes about 25% of the available CPU time. In addition to the data-acquisition tasks, the VAX also monitors a sample of the data in order to provide continuous feedback on the performance of the detector. The system saturates at the capacity of the tape units, with about equal amounts of CPU time spent on event reading, tape writing, and monitoring.

8.5 Dead-time of trigger and data acquisition

The dead-time of the trigger and readout system at a nominal intensity of 8×10^{10} protons on target in the K_L mode is about 12%. This can be categorized as follows: i) 2% comes from the synchronous part of the trigger; ii) about 2.5% comes from the encoding of the ADC information; iii) the readout of the event into the 168Es contributes a further 5%; and iv) the remaining 2.5% arises from the situation where neither of the 168E processors is able to accept a new event. Without the buffering scheme, the dead-times would be of the order of 25%. The relative contribution to the reduction of the dead-time from the FASTBUS module intermediate buffers and from the second memory after the encoding phase is a strong function of the rejection rate of the AFBI. For nominal intensity in the K_L beam, these two contributions are approximately equal.

9. CONCLUSIONS

In conclusion, Figs. 29a and 29b present an axial view of both a charged and neutral K_L two-pion decay as recorded by the various detector components. The information on the events displayed includes that from the wires recording hits in the chambers, from the pulse height in the calorimeters, as well as the reconstructed positions of the kaons, and the π^0's for the neutral decay.

Acknowledgements

We are indebted to the technical and support staffs of the participating laboratories and universities. Without their dedicated efforts, this experiment would not have been possible. In particular we would like to acknowledge the contributions of the following: i) For the construction, installation, alignment, and control of the beam: H.W. Atherton, M. Clément, G. Dubail, G. Dubois, G.P. Ferri, Ch. Lasseur, K.D. Lohmann, R. Maleyran, M.L. Mathieu and B. Tomat. ii) For the construction and operation of the helium enclosure and the wire chambers: R. Harfield, G. Juban, G. Laverrière and P. Schilly and for the development of the chamber readout: M. Roschangar and R. Seibert. iii) The support group for the liquid-argon calorimeter: P. Le Cossec, G. Fersuella, D. Guyon, G. Di Tore; and for help with the liquid-argon printed-circuit readout plane manufacture: A. Gandi. For the development of the liquid-argon calorimeter readout electronics and AFBI system: C. Arnault, A. Bellemain, R. Bernier, A. Bozzone, J.P. Coulon, J.C. Drulot, J.P. Marolleau, E. Plaige, J.P. Richer, A. Roudier. iv) For the design work on the hadron calorimeter: U. Dretzler and D. Pollmann. v) For the design of the trigger electronics: G. Antonelli, C. Avanzini, F. Morsani, P. Salvadori; for the installation of the trigger: G. Pagani and L. Zaccarelli; and for the mechanical design and construction of anticounters and hodoscope: G. Gennaro and R. Ruberti. vi) For help with the CFI: D. Jacobs, R. McLaren, E.M. Rimmer, C. Bizeau, P. Ponting and A. Lovell; for design and construction of the Block Mover: L. Pregernig; for work on the 168E system: G. Iksal; and for help with the data acquisition: A. Lacourt.

+) Institut für Physik, Univ. Dortmund, Fed. Rep. Germany, funded by the German Federal Ministry for Research and Technology (BMFT) under contract number 053DO41.

Physics Dept., Univ. Edinburgh, UK, supported by the UK Science and Engineering Research Council.

Institut für Physik, Universität Mainz, Fed. Rep. Germany, funded by the German Federal Ministry for Research and Technology (BMFT) under contract number 054MZ18.

LAL, Univ. Paris-Sud, Orsay, France, supported by the Institut National de Physique Nucléaire et de Physique des Particules.

Sezione INFN and Dipartimento di Fisica, Pisa, Italy, supported by the National Institute of Nuclear Research (INFN).

Fachbereich Physik, Universität-Gesamthochschule Siegen, Fed. Rep. Germany, supported by the German Federal Ministry for Research and Technology under contract number 054SI74.

REFERENCES

[1] J. Cronin, Rev. Mod. Phys. **53** (1981) 373.
L.L. Chau, Phys. Rep. **95** (1983) 1.
L. Wolfenstein, Ann. Rev. Nucl. Sci. **36** (1986) 137.

[2] J.K. Black et al., Phys. Rev. Lett. **54** (1985) 1628.
R.H. Bernstein et al., Phys. Rev. Lett. **54** (1985) 1631.

[3] D. Cundy et al., proposal P174, CERN/SPSC/81-110 (1981), unpublished.

[4] C. Cerri et al. (INFN Pisa), The neutral hodoscope for the CERN CP violation experiment, in preparation (1987).

[5] H. Cunitz, W. Sippach and J.H. Dieperink, Nucl. Instrum. Methods **91** (1971) 211.

[6] G. Kesseler, Liquid-argon calorimeter hardware, NA31 Note 22 (1987).
C. Arnault et al., CERN NA31 Note 86-032, Orsay (1986).

[7] R.L. Chase and J.P. Richer, IEEE Trans. Nucl. Sci. **NS-31** (1) (1984) 258.

[8] A. Bellemain et al., IEEE Trans. Nucl. Sci. **NS-32** (4) (1985) 1339.

[9] R. Ford and W. Nelson, report SLAC-210 (1978).

[10] A. Fucci et al., Nucl. Instrum. Methods **147** (1987) 587.

[11] P.F. Kunz et al., Nucl. Instrum. Methods **9** (1976) 435.
M. Rost et al., Nucl. Instrum. Methods **242** (1985) 153.

[12] IEEE Standard FASTBUS Modular High-Speed Data Acquisition and Control System, ANSI/IEEE STD 960-1986 (1986).

[13] J. Pregernig, IEEE Trans. Nucl. Sci. **NS-33** (1) (1986) p. 797

[14] D. Jacobs et al., CAMAC FASTBUS Interface, internal report CERN DD: FB/MAN1, December 1983.

[15] C. Arnault et al., Proc. Conf. on Computing in High-Energy Physics, Amsterdam, 1985 (North-Holland, Amsterdam, 1986), p. 231.

Table 1

Parameters of K_L and K_S beams

	K_L beam	K_S beam
Length of beam from target to:		
defining collimator (m)	48.0	
exit of final coll. (m)	120.0	7.1
Distance: final collimator to the argon calorimeter (m)	123.8	124.7 to 76.7
Target:		
material	Be	Be
length (m)	0.4	0.4
diameter (mm)	2.0	2.0
Production angle (mrad)	3.6	3.6
Beam acceptance:		
angle (mrad)	± 0.2	± 0.5
solid angle (sr)	$4\pi \times 10^{-8}$	$25\pi \times 10^{-8}$
Primary proton beam (450 GeV/c) incident on target:		
nominal flux per SPS pulse	1×10^{11}	3×10^{7}
K^0 in beam at production:		
calculated flux per pulse (from Ref. 3)	1.8×10^{6}	3.3×10^{3}
Neutrons in beam:		
estimated flux per pulse	$\approx 1.5 \times 10^{7}$	$\approx 3 \times 10^{4}$

Table 2

Typical counting rates recorded by the detector with K_L and K_S beams

Beam mode	Charged particle flux	Muon flux	Non-penetrating particle flux
K_L: 1×10^{11} protons per pulse on target	2.5×10^{5}	0.8×10^{5} [a)]	1.7×10^{5}
K_S: 3×10^{7} protons per pulse on target, K_S anticounter in beam (Station 21)	2.0×10^{5}	0.2×10^{5}	1.8×10^{5}

a) The contribution to the muon counting rate originating from the K_L production target and proton beam dump was calculated to be 0.5×10^{5} per 10^{11} protons using the program HALO [C. Iselin, CERN 74-17 (1974)].

Table 3

Design parameters and performance figures
of the liquid-argon calorimeter

Size of the Pb/Al sandwich plates (mm)	1204 × 2408 × 2.3
Size of the readout plates (mm)	1200 × 2400 × 0.8
Weight of a sandwich plate (kg)	≈ 55
Weight of a readout plate (kg)	≈ 5.2
Length of one cell (mm)	7.3
Number of cells	80
Length of calorimeter package including scintillator plane (mm)	608
Number of channels	1536
Internal dimensions of liquid-argon vessel (w × h × ℓ)	2840 × 3687 × 50
Liquid-argon volume (with cal. package in place) (l)	≈ 4300
External dimensions of vacuum vessel (w × h × ℓ) (mm)	3350 × 3900 × 1160
Overall diameter of windows (mm)	2830
Thickness of entry (exit) window (mm)	150 (120)
Overall length window-to-window (mm)	1190
Beam tube inner diameter (mm)	192
Number of rad. lengths of one cell	0.32
Number of rad. lengths of calorimeter package	≈ 25
Number of rad. lengths of total calorimeter	≈ 27
Number of rad. lengths before first cell	0.90
Energy resolution (E in GeV)	$7.5\%/\sqrt{E}$
Typical space resolution (mm)	1.0

Table 4

Rejection efficiency of the AFBI

	K_L beam	K_S beam
Events with only a neutral trigger:		
$E_{\text{argon calorimeter}} > 44$ GeV	0.30	0.23
Centre of gravity:		
$x < 15$ cm	0.15	0.18
$y < 15$ cm	0.18	0.35
$z_{\text{vertex}} < 50$ m	0.76	0.54
Combined rejection	0.84	0.54
Events with only a charged trigger:		
$E_{\text{total}} > 35$ GeV	0.33	0.07
$E_{\text{had calorimeter}} > 1.6$ GeV	0.03	0.006
Electron rejection $\text{MAX}[F/(B+H)] < 4$	0.05	0.007
Combined rejection	0.41	0.075
Overall rejection[a)]	0.50	0.30

a) This includes 15% of input events which are not rejected because they either satisfy both the neutral and charged triggers, or are down-scaled events.

Figure captions

Fig. 1a: Schematic layout of K_L/K_S beams, decay region, and detectors.

Fig. 1b: Schematic layout of detector elements.

Fig. 2: K_L target station and beam.

Fig. 3: K_S beam train.

Fig. 4: Momentum spectrum of K_S at the target for 10^7 incident protons.

Fig. 5:
a) Element of ring anticounter with scintillator and Fe conversion plates.
b) Anticounter rings 1 and 2.
c) Anticounter rings 3 and 4.

Fig. 6: Scintillator hodoscope plane for charged decay t_0.

Fig. 7: Scintillator plane for neutral decay t_0.

Fig. 8: Expanded view of the relative wire spacing in the four planes of a wire chamber.

Fig. 9: Mechanical assembly of the wire chamber frames.

Fig. 10: Block diagram of the wire chamber electronics.

Fig. 11: Dimensions and general layout of the liquid-argon calorimeter.

Fig. 12: Cell structure of liquid-argon calorimeter.

Fig. 13: Section of the low-impedance flat cable.

Fig. 14: Exploded view of the main cryostat elements (schematic).

Fig. 15: The cooling systems.

Fig. 16:
a) Liquid-argon calorimeter preamplifier output signal in arbitrary units. In circuit: C_d is detector capacitance; R_S is the terminating resistance; C_a and R_a are the preamplifier input capacitance and resistance, respectively; and n is the transformer turns ratio.
b) Cross-talk signal in the same units as Fig. 16a.

Fig. 17:
a) Sample-and-hold charge measurement of calorimeter signals.
b) Schematic of sample-and-hold. With successive opening of switches S_A, S_B, and S_C, three measured charges are stored on capacitors C_A, C_B, and C_C. These are combined as in Fig. 17a and stored on C_{II}.

Fig. 18: Energy response for 15 and 80 GeV electrons.

Fig. 19: Energy resolution versus energy for electrons.

Fig. 20: Distance between the measured and the extrapolated position of electron showers in K_{e3} decays for electron energy > 25 GeV.

Fig. 21: The π^0 mass peak in the decay $K_S \to \pi^0\pi^0$. The resolution is 2.2 MeV (or 1.6%).

Fig. 22: $K_S \to \pi^0\pi^0$ vertex distribution with superimposed fit to the anticounter position.

Fig. 23: The hadron calorimeter.

Fig. 24: Laser calibration system for the hadron calorimeter.

Fig. 25: Reconstructed pion energy distributions for 20, 80, and 120 GeV/c.

Fig. 26: Hadronic energy resolution versus hadron (pion) energy.

Fig. 27: Configuration of data-acquisition system.
Key to FASTBUS modules:

ADC		F6829
FBAP	ADC memory	F6828
FAS	Fast sequencer	F6827
PU	192-bit registers	F680C
TDC		F680B
SCA	Scaler unit	F680C
WCA	Wire chamber address unit	F6813
MSL	ADC memory link	F682A
HTM	Logic state analysers	F680D

SI	Segment interconnect	F1010, F0080
CFI	CERN FASTBUS interface	F680F
BM	Block mover	F6809
ALC	Cable ancillary logic	F6842, F1002

Fig. 28: IBM 168 emulator system.

Fig. 29: Event display of a) $K_L \rightarrow \pi^+\pi^-$ and b) $K_L \rightarrow \pi^0\pi^0 \rightarrow 4\gamma$ as seen along the beam axis. Included are the reconstructed positions of pions, photons, and kaons:

WC1,2	Wire chambers 1 and 2,
LAC(F,B)	Liquid-argon calorimeter, front and back,
HAC(F,B)	Hadron calorimeter, front and back.

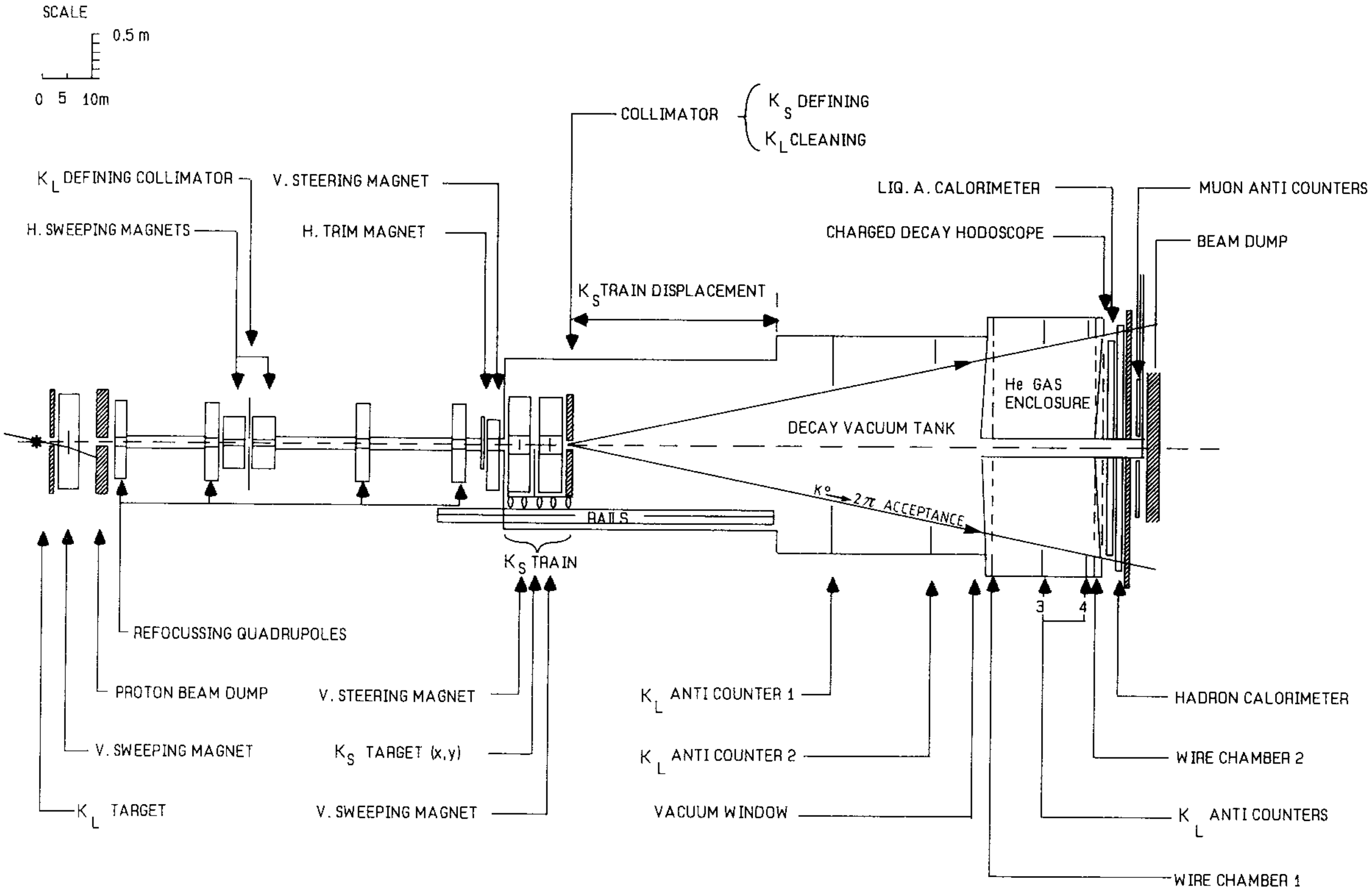
SCALE
0.5 m
0 5 10m
COLLIMATOR
K_S DEFINING
K_L CLEANING
K_L DEFINING COLLIMATOR
V. STEERING MAGNET
H. SWEEPING MAGNETS
H. TRIM MAGNET
K_S TRAIN DISPLACEMENT
LIQ. A. CALORIMETER
MUON ANTI COUNTERS
CHARGED DECAY HODOSCOPE
BEAM DUMP
He GAS ENCLOSURE
DECAY VACUUM TANK
$K^\circ \rightarrow 2\pi$ ACCEPTANCE
RAILS
K_S TRAIN
3
4
REFOCUSSING QUADRUPOLES
PROTON BEAM DUMP
V. SWEEPING MAGNET
K_L TARGET
V. STEERING MAGNET
K_S TARGET (x,y)
V. SWEEPING MAGNET
K_L ANTI COUNTER 1
K_L ANTI COUNTER 2
VACUUM WINDOW
HADRON CALORIMETER
WIRE CHAMBER 2
K_L ANTI COUNTERS
WIRE CHAMBER 1

fig. 1a

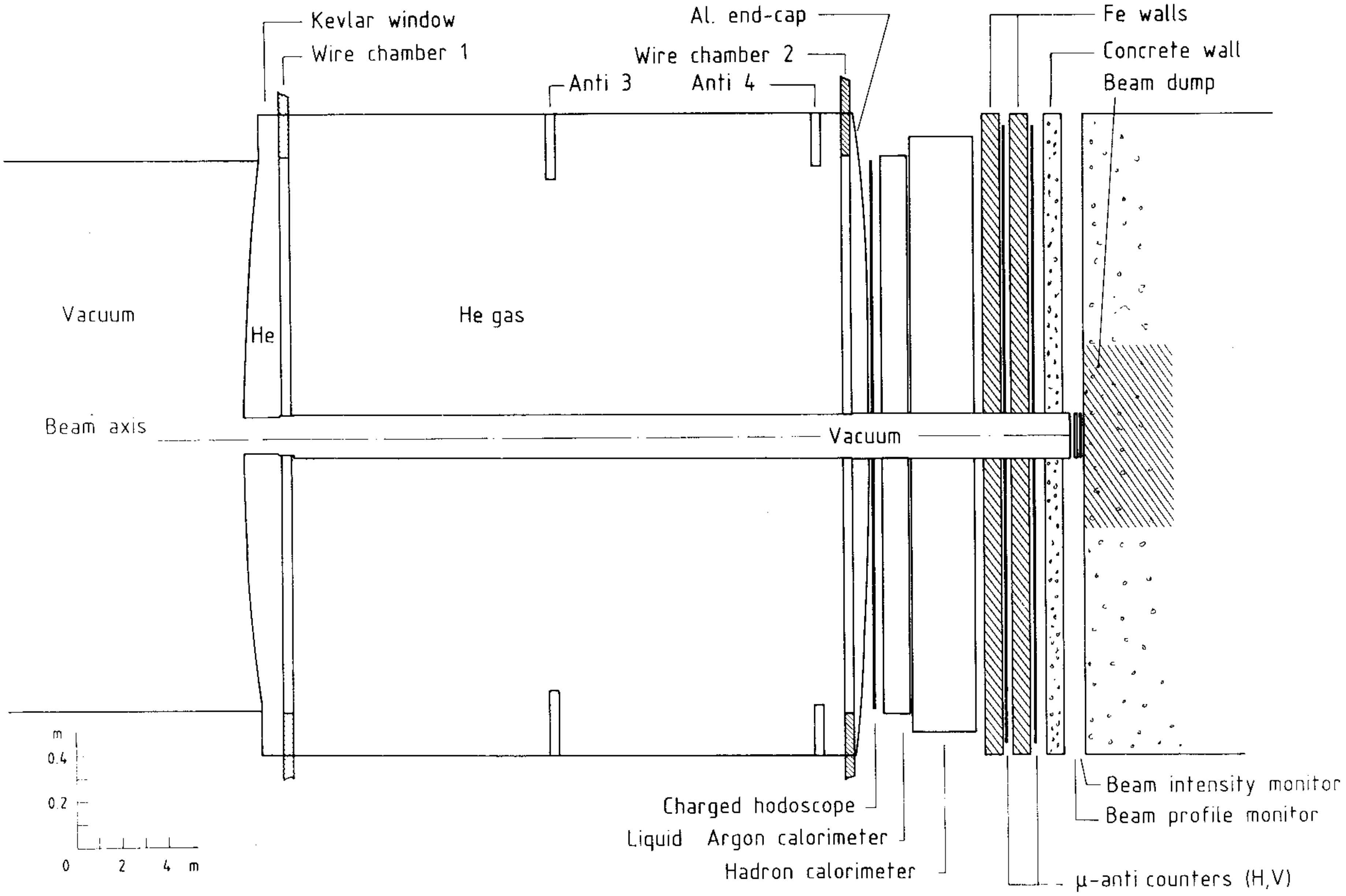
Kevlar window
Wire chamber 1
Anti 3
Wire chamber 2
Anti 4
Al. end-cap
Fe walls
Concrete wall
Beam dump
Vacuum
He
He gas
Beam axis
Vacuum
m
0.4
0.2
0
2
4
m
Charged hodoscope
Liquid Argon calorimeter
Hadron calorimeter
μ-anti counters (H,V)
Beam intensity monitor
Beam profile monitor

fig. 1b

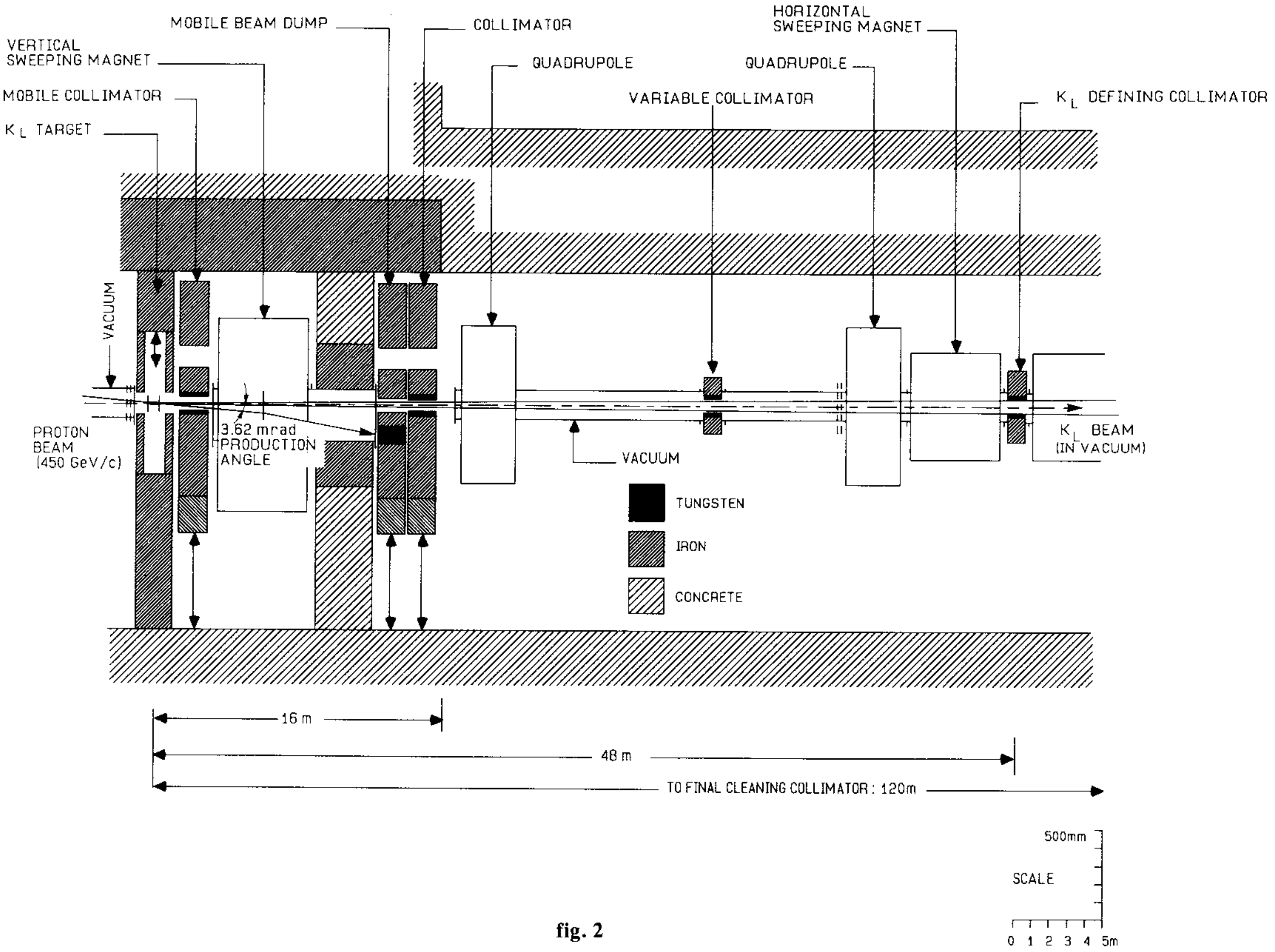

VERTICAL SWEEPING MAGNET
MOBILE BEAM DUMP
COLLIMATOR
HORIZONTAL SWEEPING MAGNET
MOBILE COLLIMATOR
QUADRUPOLE
QUADRUPOLE
VARIABLE COLLIMATOR
K_L TARGET
K_L DEFINING COLLIMATOR
VACUUM
PROTON BEAM (450 GeV/c)
3.62 mrad PRODUCTION ANGLE
VACUUM
K_L BEAM (IN VACUUM)
TUNGSTEN
IRON
CONCRETE
16 m
48 m
TO FINAL CLEANING COLLIMATOR : 120m
500mm
SCALE
0 1 2 3 4 5m

fig. 2

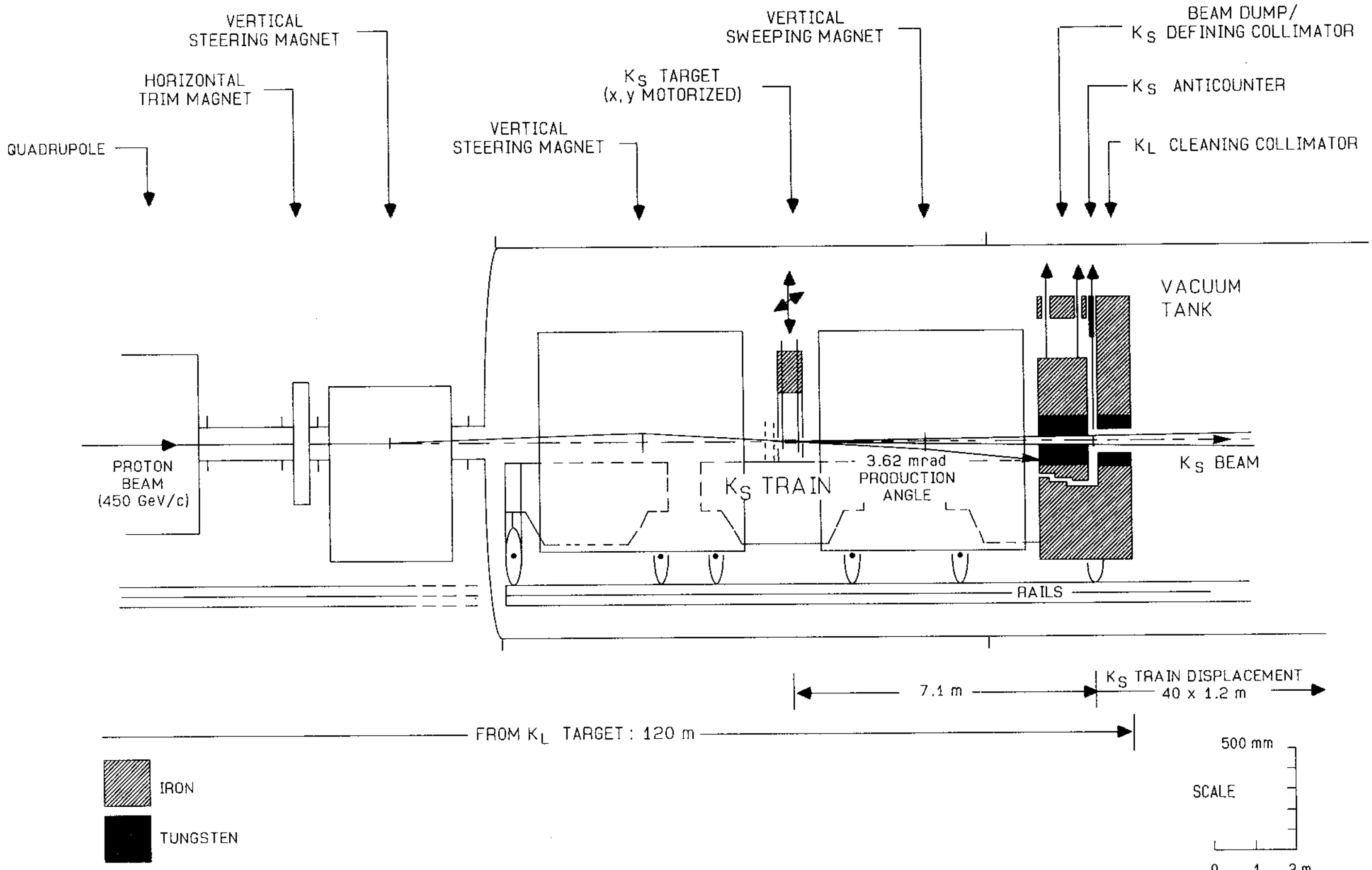
QUADRUPOLE
HORIZONTAL TRIM MAGNET
VERTICAL STEERING MAGNET
VERTICAL STEERING MAGNET
K_S TARGET (x, y MOTORIZED)
VERTICAL SWEEPING MAGNET
BEAM DUMP/ K_S DEFINING COLLIMATOR
K_S ANTICOUNTER
K_L CLEANING COLLIMATOR
VACUUM TANK
PROTON BEAM (450 GeV/c)
K_S TRAIN
3.62 mrad PRODUCTION ANGLE
K_S BEAM
RAILS
7.1 m
K_S TRAIN DISPLACEMENT 40 x 1.2 m
FROM K_L TARGET : 120 m
IRON
TUNGSTEN
500 mm
SCALE
0
1
2 m

fig. 3

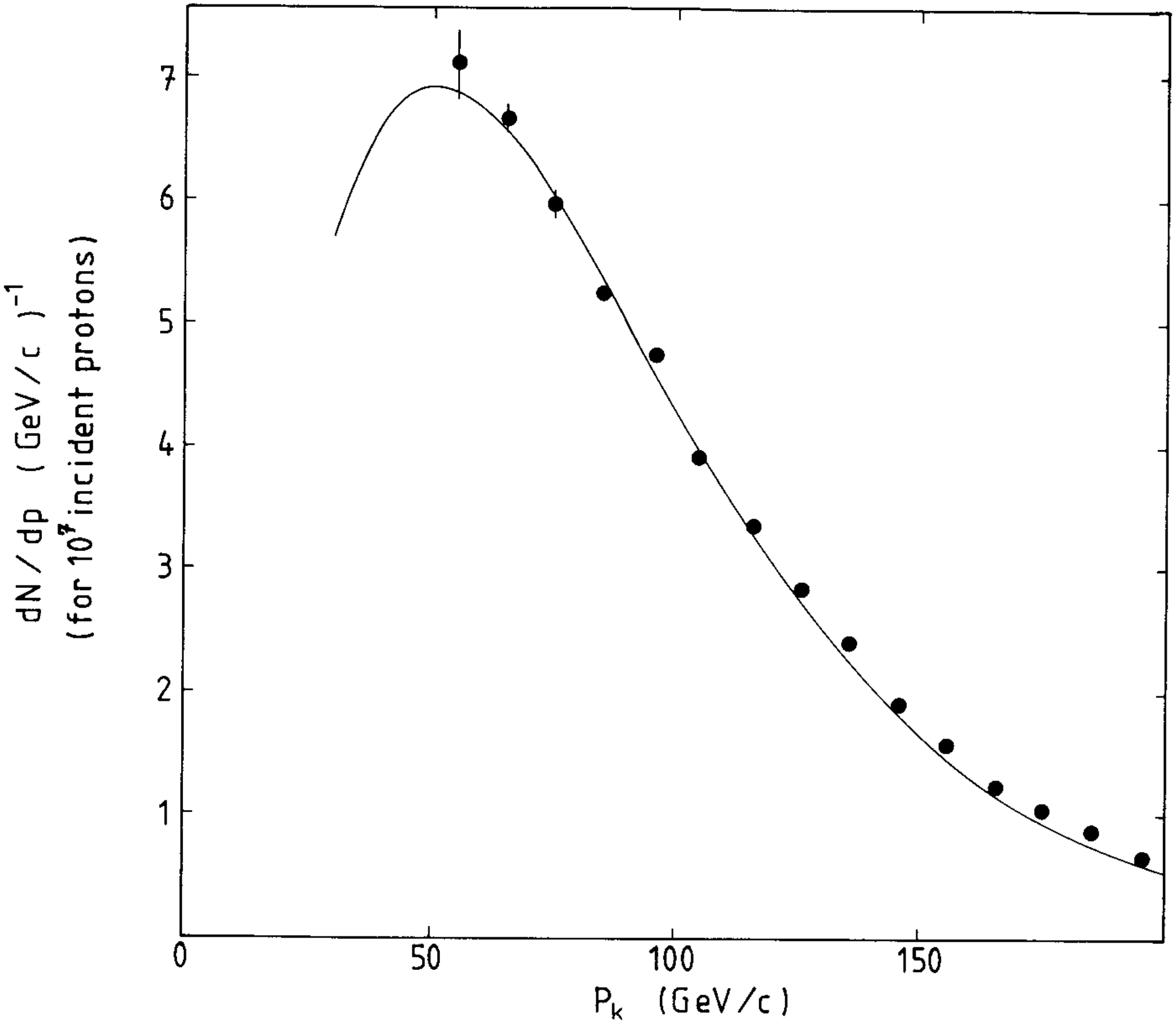
dN / dp (GeV / c)$^{-1}$
(for 10^{7} incident protons)
1
2
3
4
5
6
7
0
50
100
150
P_k (GeV / c)

fig. 4

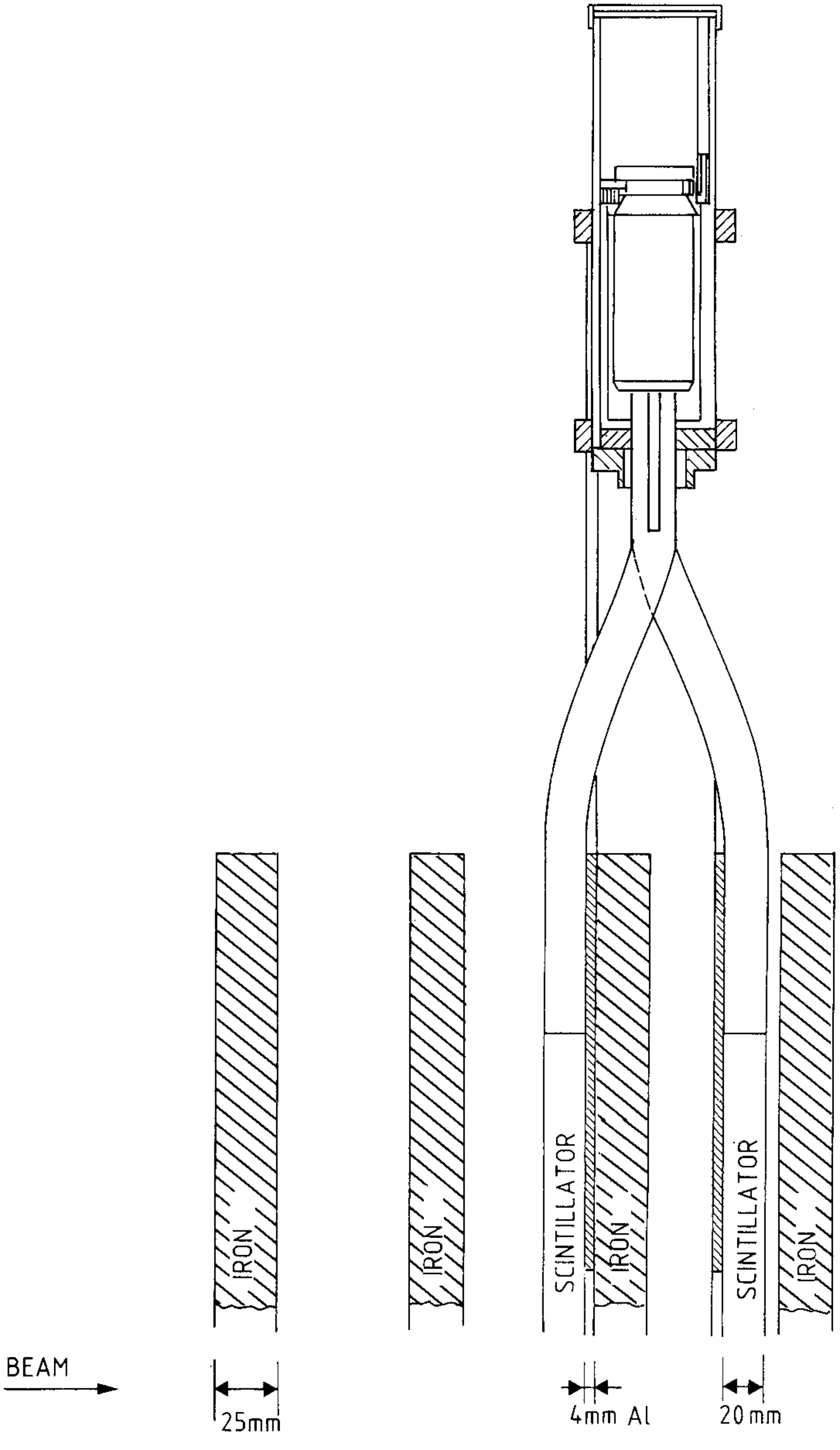
IRON
IRON
SCINTILLATOR
IRON
SCINTILLATOR
IRON
BEAM
25mm
4mm Al
20mm

fig. 5a

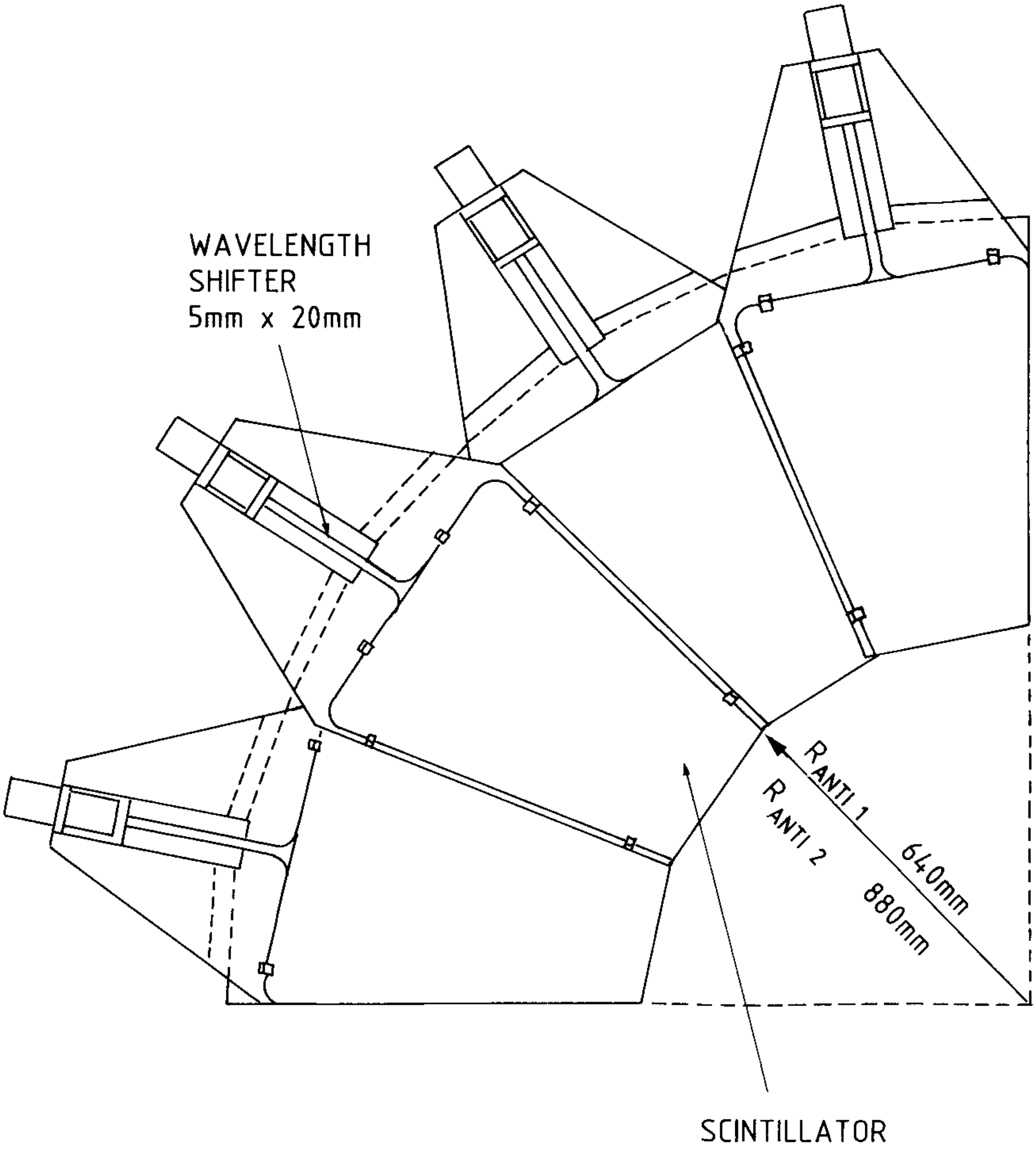
WAVELENGTH
SHIFTER
5mm x 20mm
$R_{ANTI\,1}$ 640mm
$R_{ANTI\,2}$ 880mm
SCINTILLATOR

fig. 5b

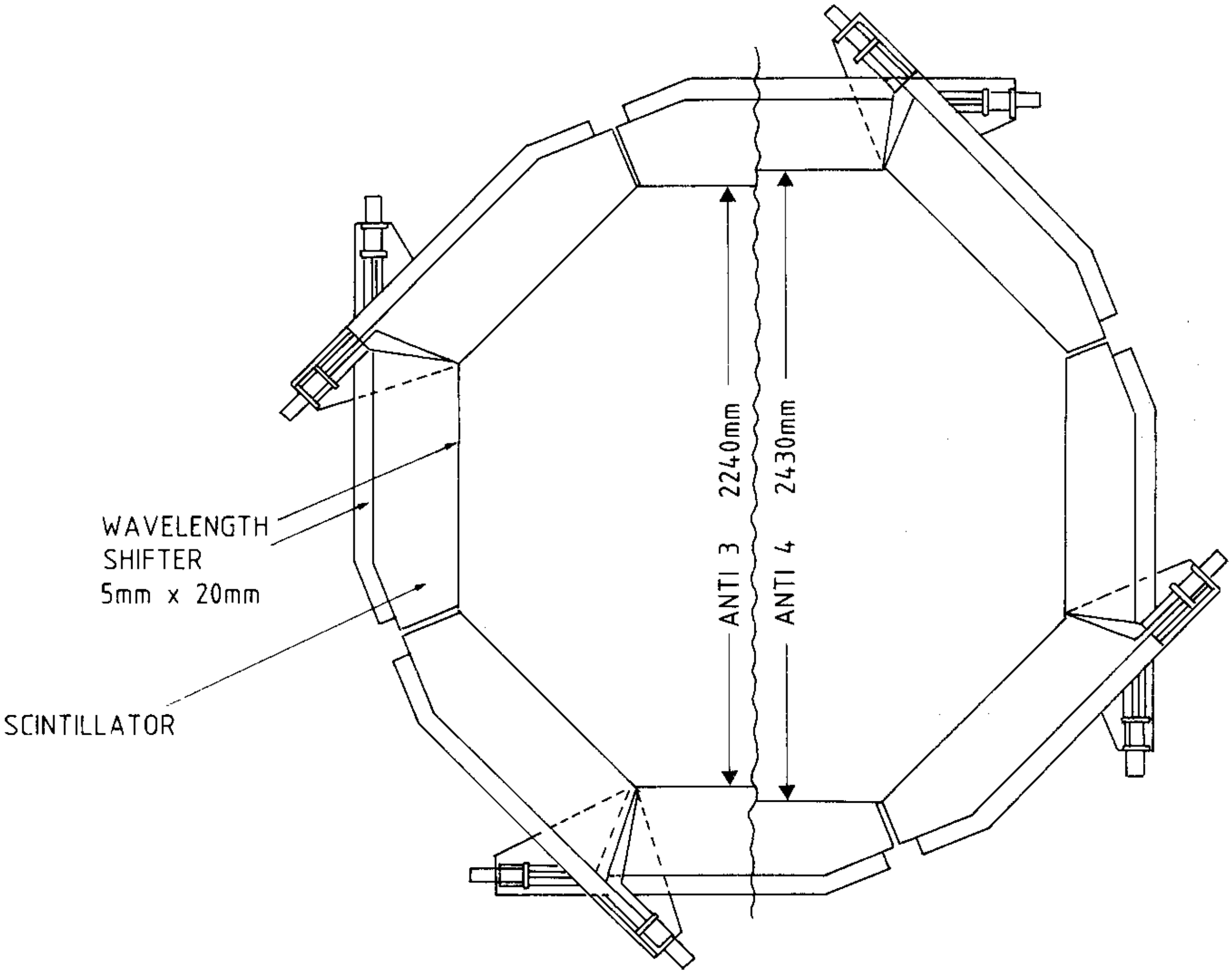
WAVELENGTH
SHIFTER
5mm x 20mm
SCINTILLATOR
ANTI 3 2240mm
ANTI 4 2430mm

fig. 5c

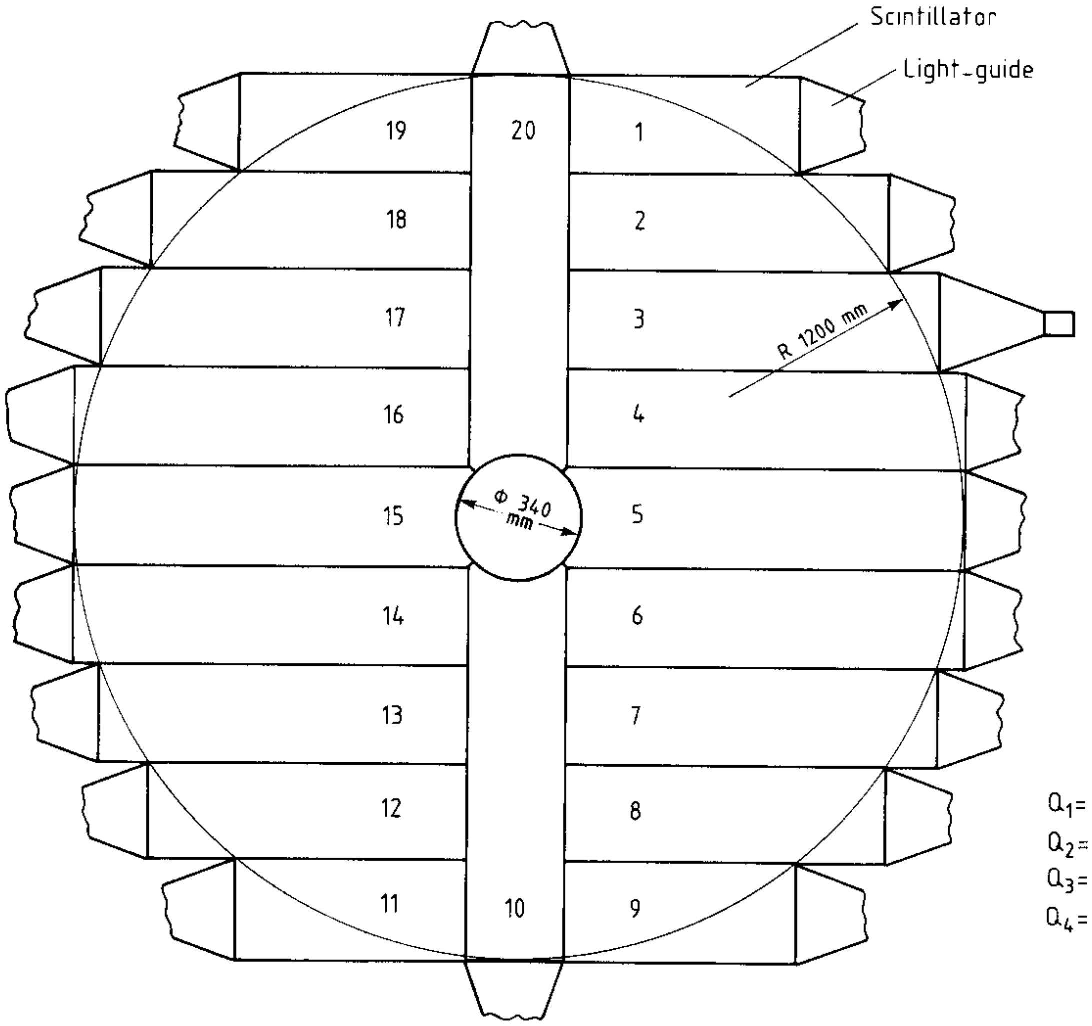

$Q_1 = 1+2+3+4+5+20$

$Q_2 = 5+6+7+8+9+10$

$Q_3 = 10+11+12+13+14+15$

$Q_4 = 15+16+17+18+19+20$

fig. 6

Charged decays:

$t_0 = Q_1 \cdot Q_3 + Q_2 \cdot Q_4$

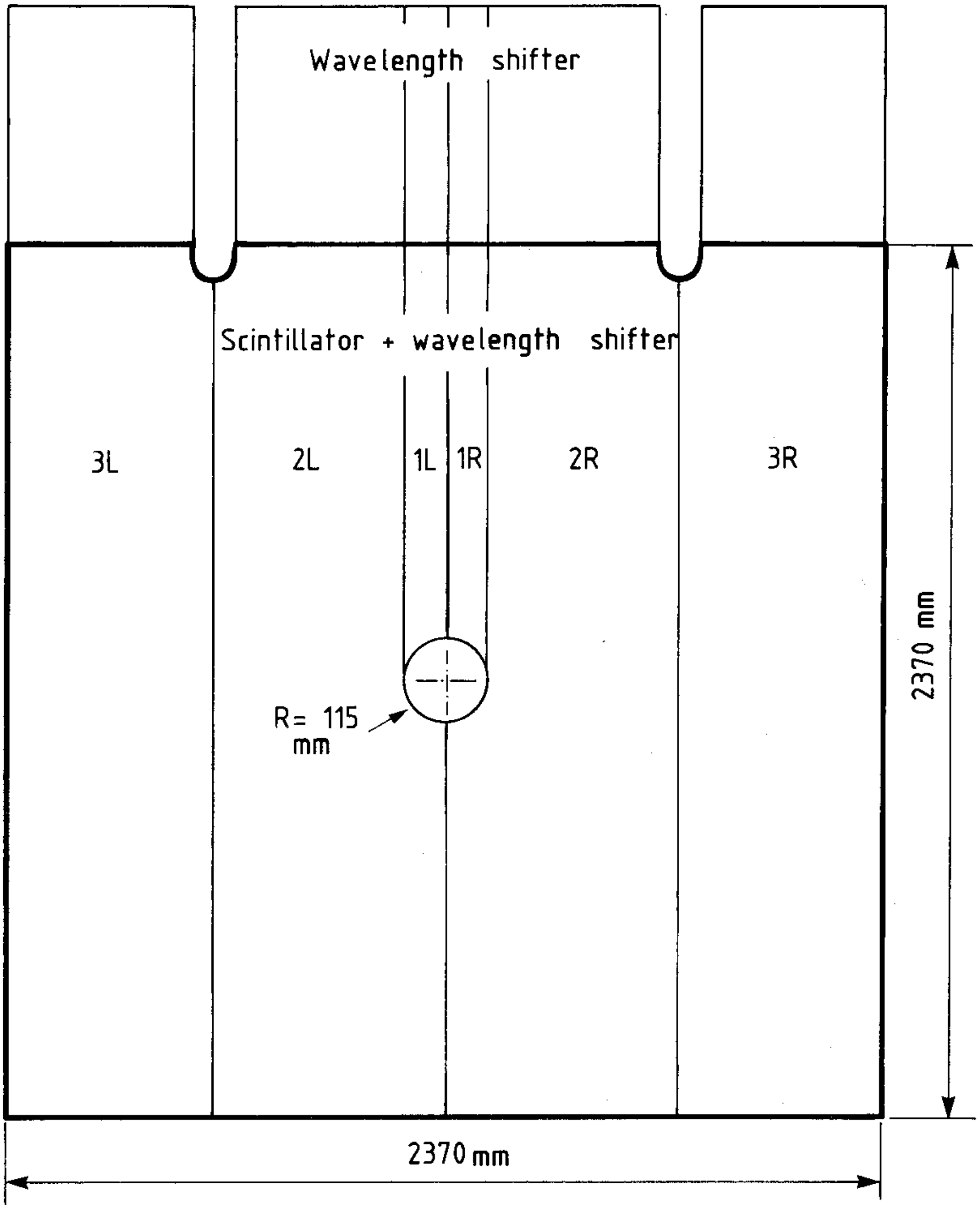

Neutral decays:

$t_0 = (1R + 2R + 3R) \bullet (1L + 2L + 3L) + 1R \bullet 2R + 1L \bullet 2L$

fig. 7

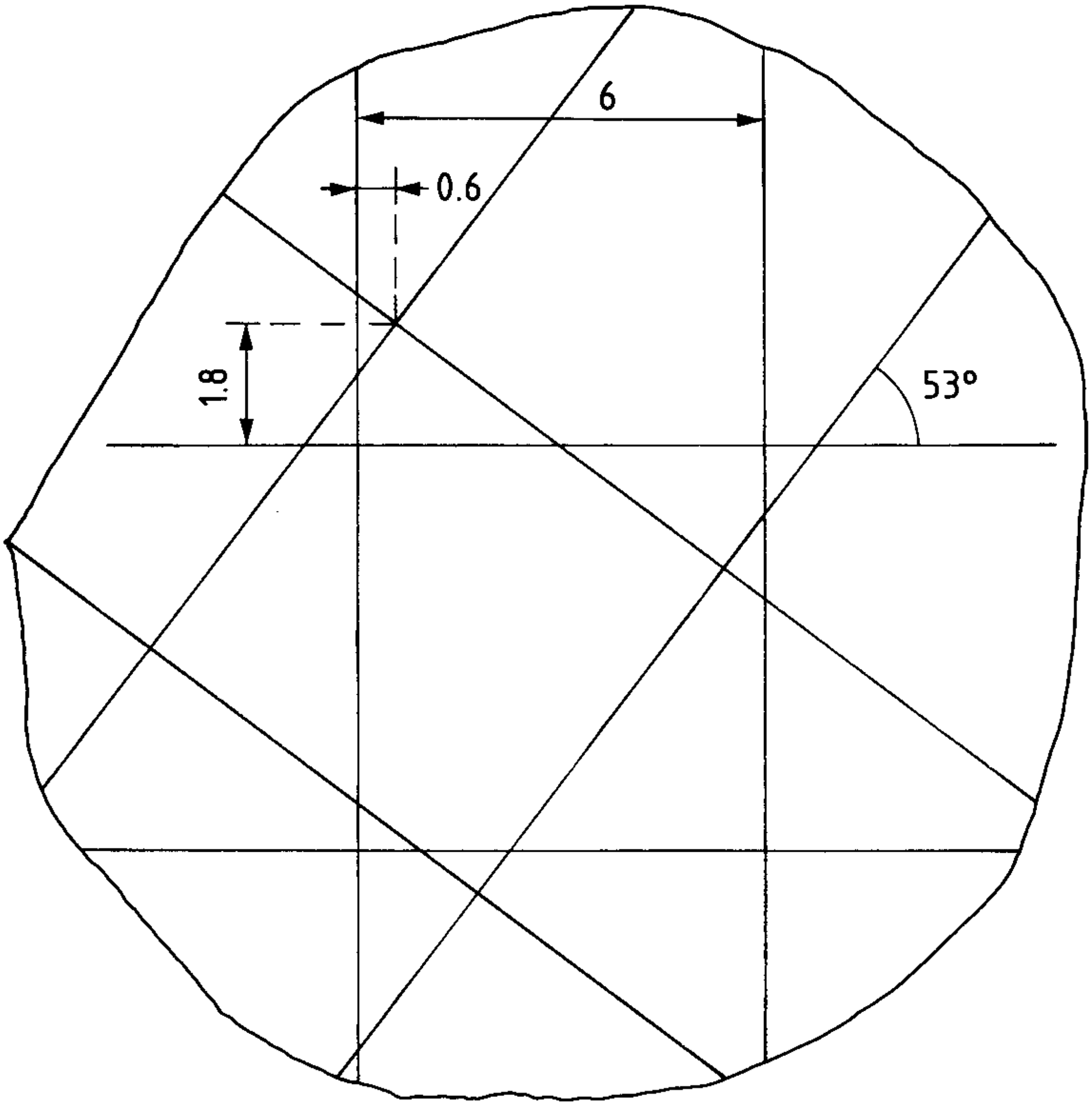

fig. 8

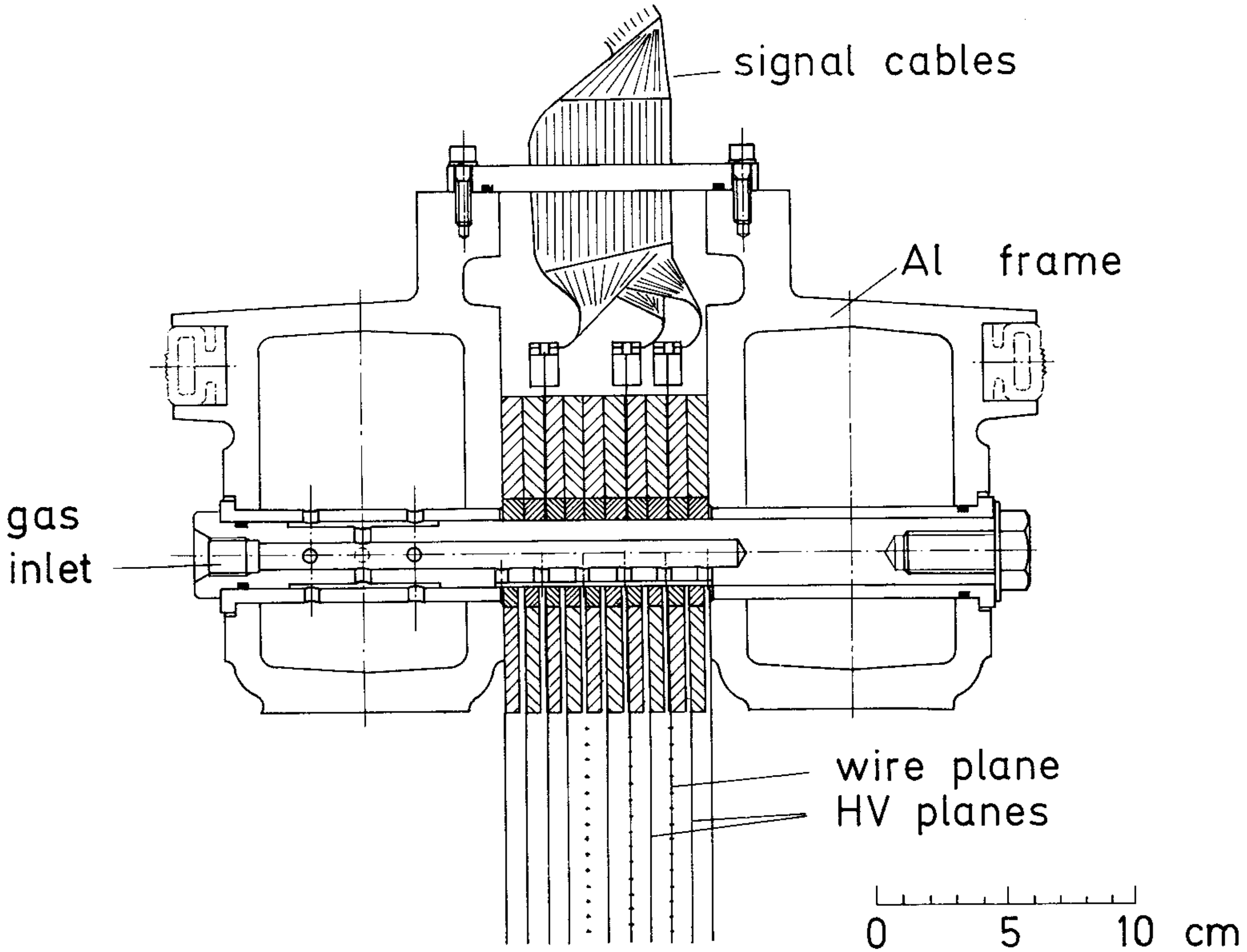
signal cables
Al frame
gas inlet
wire plane
HV planes
0
5
10 cm

fig. 9

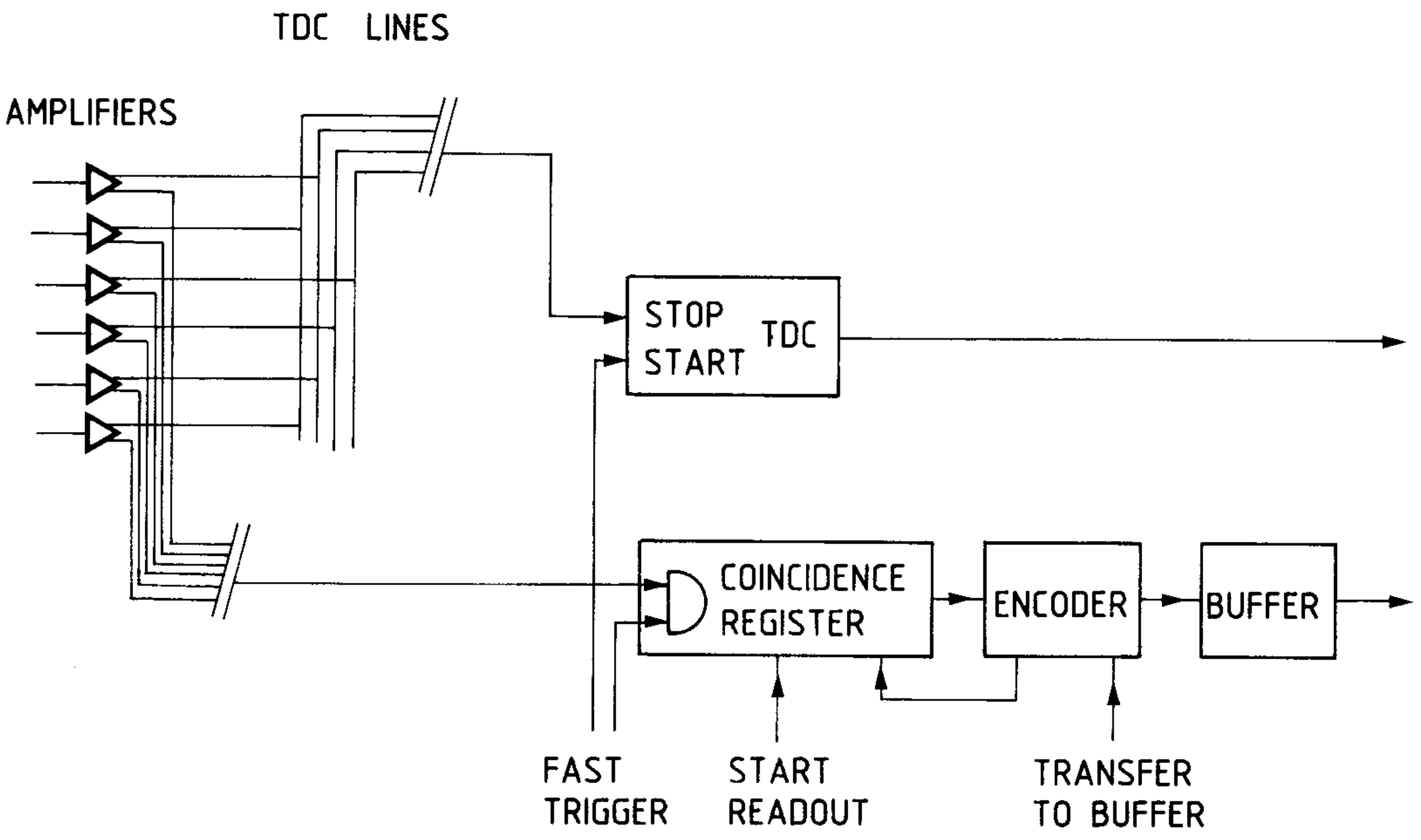
TDC LINES
AMPLIFIERS
STOP
START
TDC
COINCIDENCE
REGISTER
ENCODER
BUFFER
FAST
TRIGGER
START
READOUT
TRANSFER
TO BUFFER

fig. 10

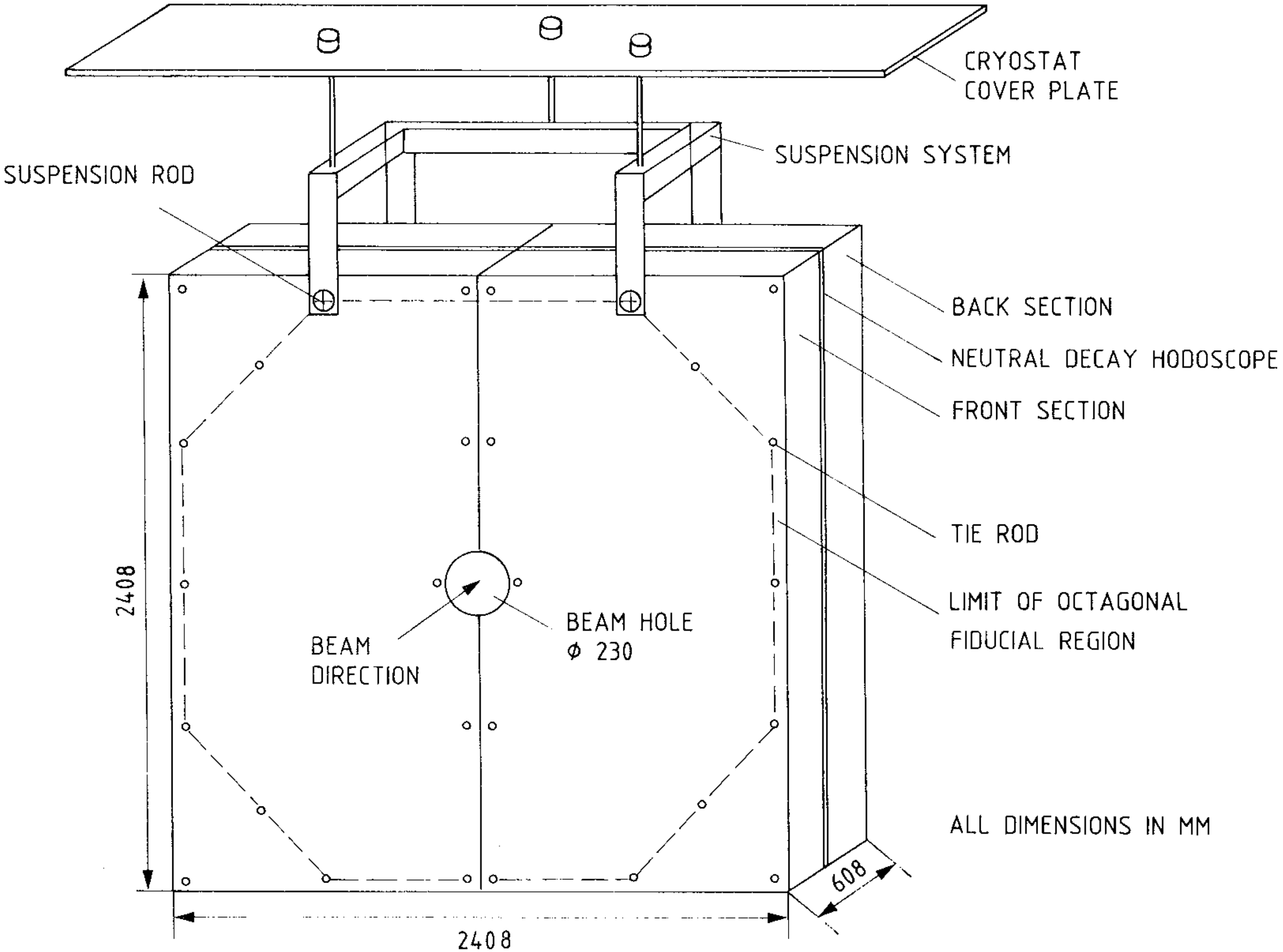
CRYOSTAT
COVER PLATE
SUSPENSION SYSTEM
SUSPENSION ROD
BACK SECTION
NEUTRAL DECAY HODOSCOPE
FRONT SECTION
TIE ROD
LIMIT OF OCTAGONAL
FIDUCIAL REGION
BEAM HOLE
ϕ 230
BEAM
DIRECTION
ALL DIMENSIONS IN MM
2408
2408
608

fig. 11

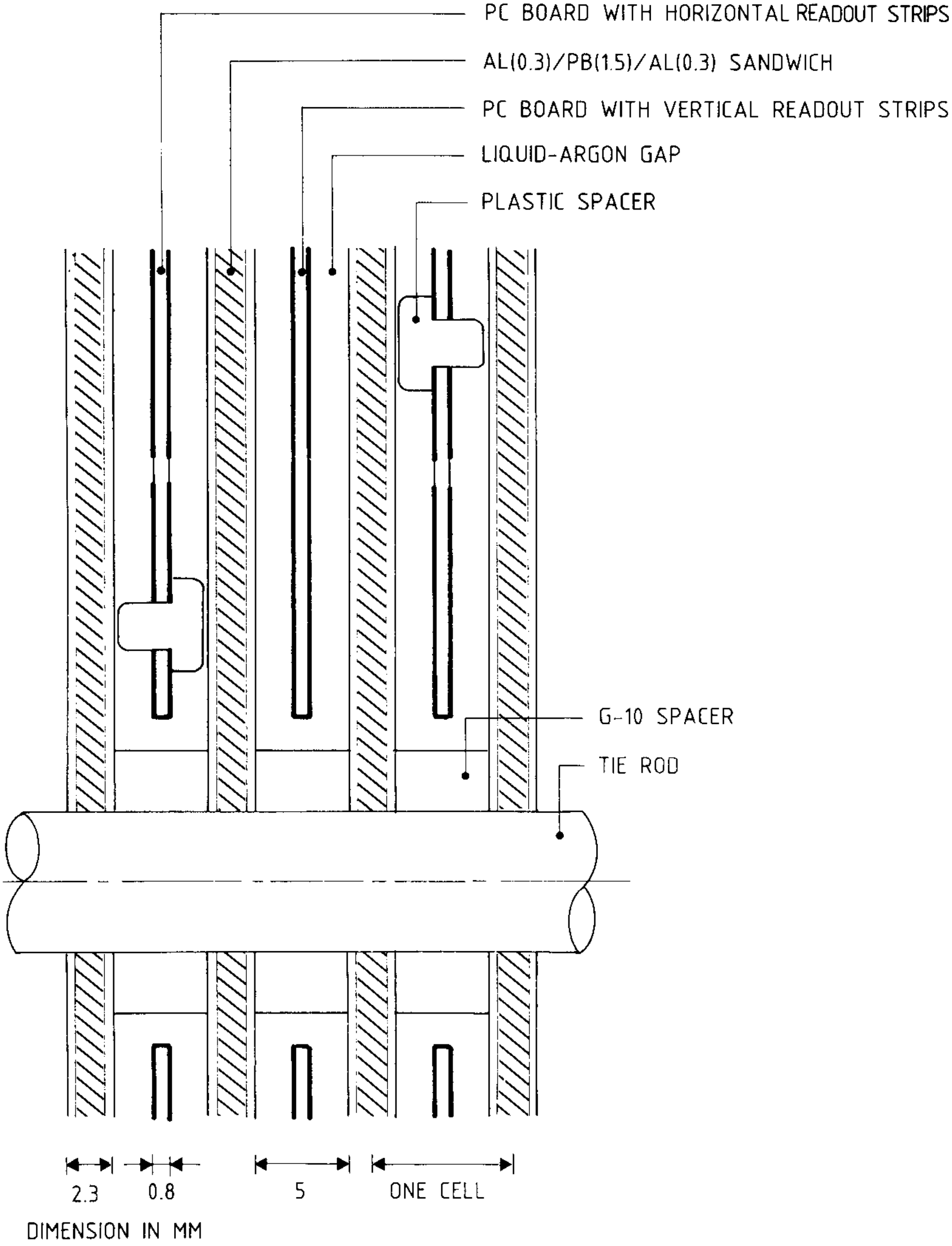
PC BOARD WITH HORIZONTAL READOUT STRIPS
AL(0.3)/PB(1.5)/AL(0.3) SANDWICH
PC BOARD WITH VERTICAL READOUT STRIPS
LIQUID-ARGON GAP
PLASTIC SPACER
G-10 SPACER
TIE ROD
2.3
0.8
5
ONE CELL
DIMENSION IN MM

fig. 12

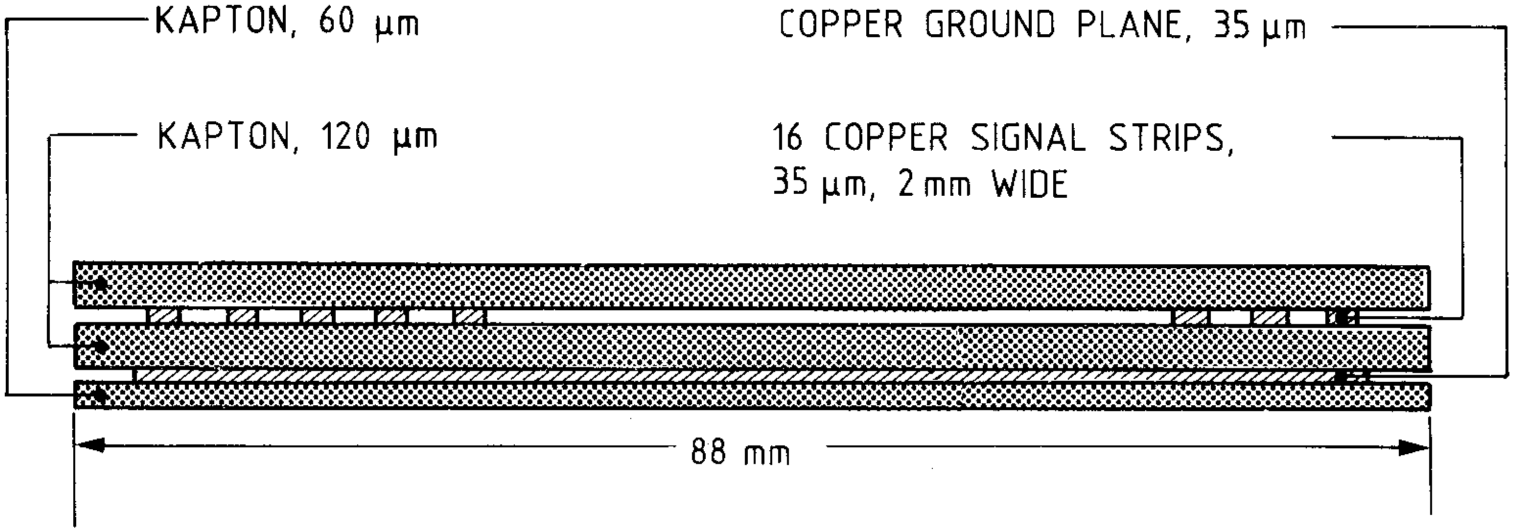
KAPTON, 60 µm
KAPTON, 120 µm
COPPER GROUND PLANE, 35 µm
16 COPPER SIGNAL STRIPS,
35 µm, 2 mm WIDE
88 mm

fig. 13

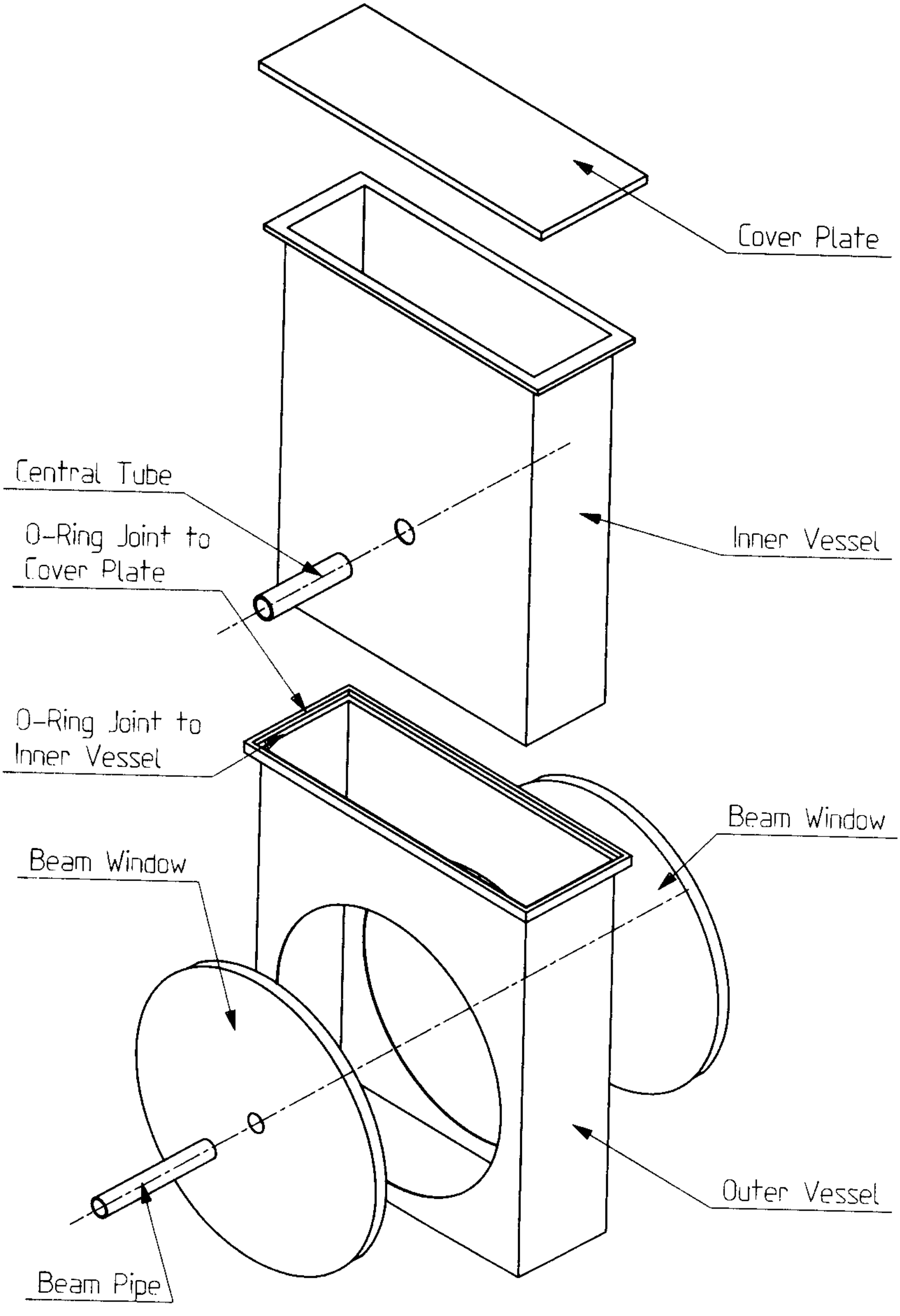
Cover Plate
Central Tube
O-Ring Joint to
Cover Plate
Inner Vessel
O-Ring Joint to
Inner Vessel
Beam Window
Beam Window
Outer Vessel
Beam Pipe

fig. 14

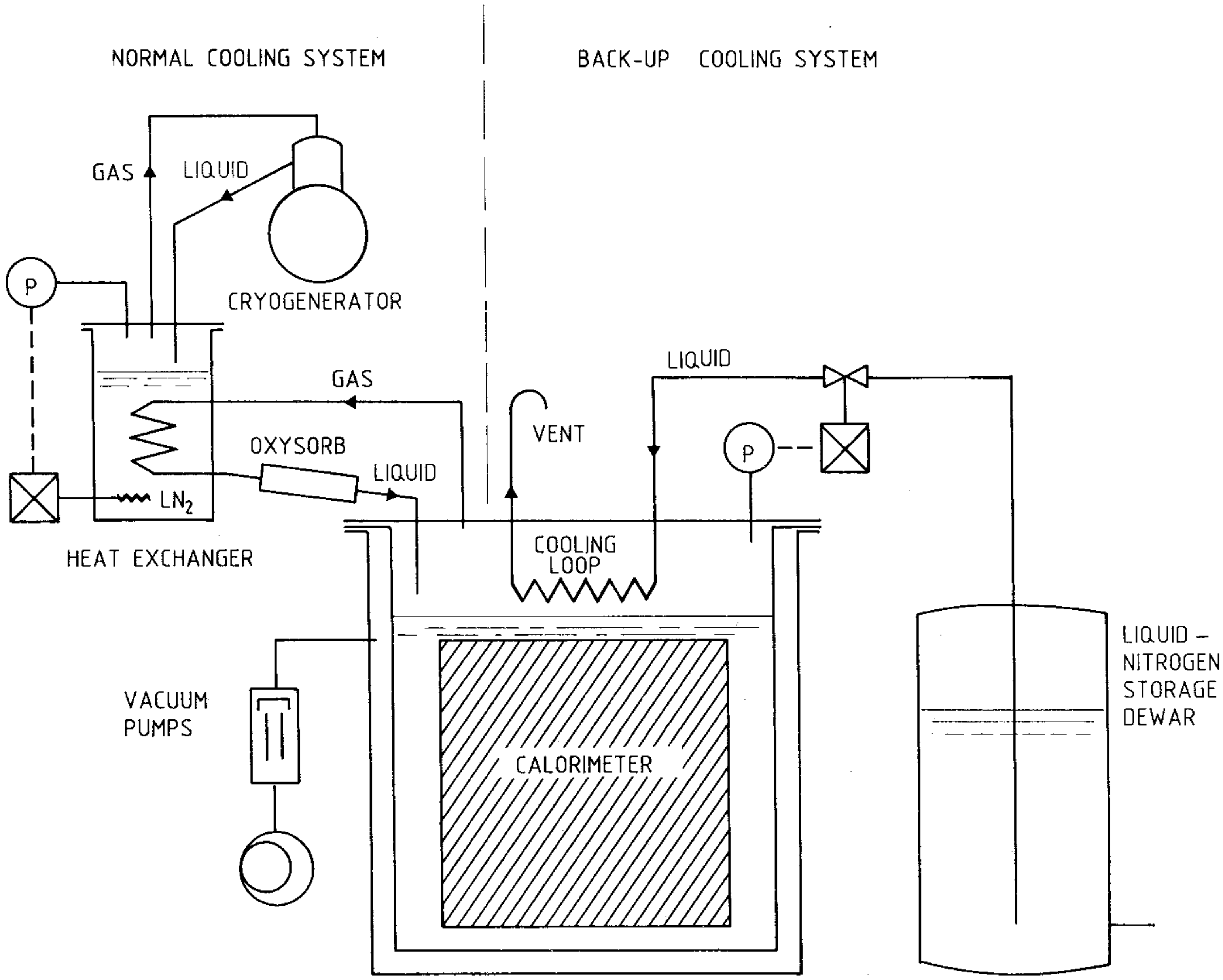
NORMAL COOLING SYSTEM
BACK-UP COOLING SYSTEM
GAS
LIQUID
P
CRYOGENERATOR
GAS
OXYSORB
LIQUID
LN_2
HEAT EXCHANGER
VENT
LIQUID
P
COOLING LOOP
VACUUM PUMPS
CALORIMETER
LIQUID - NITROGEN STORAGE DEWAR

fig. 15

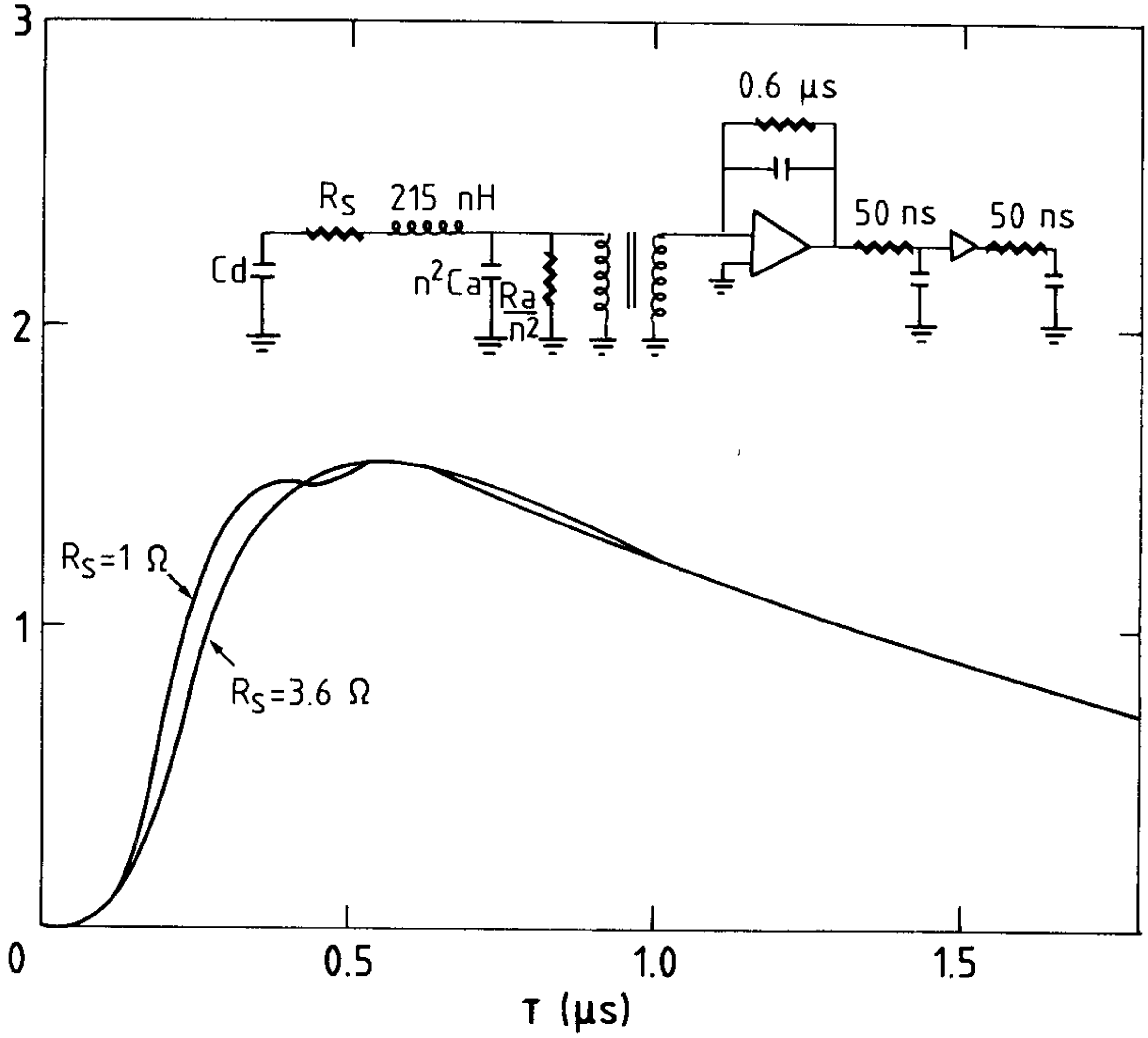
3
2
1
0
0.5
1.0
1.5
T (μs)
0.6 μs
R_S
215 nH
Cd
n^2Ca
$\frac{Ra}{n^2}$
50 ns
50 ns
R_S=1 Ω
R_S=3.6 Ω

fig. 16a

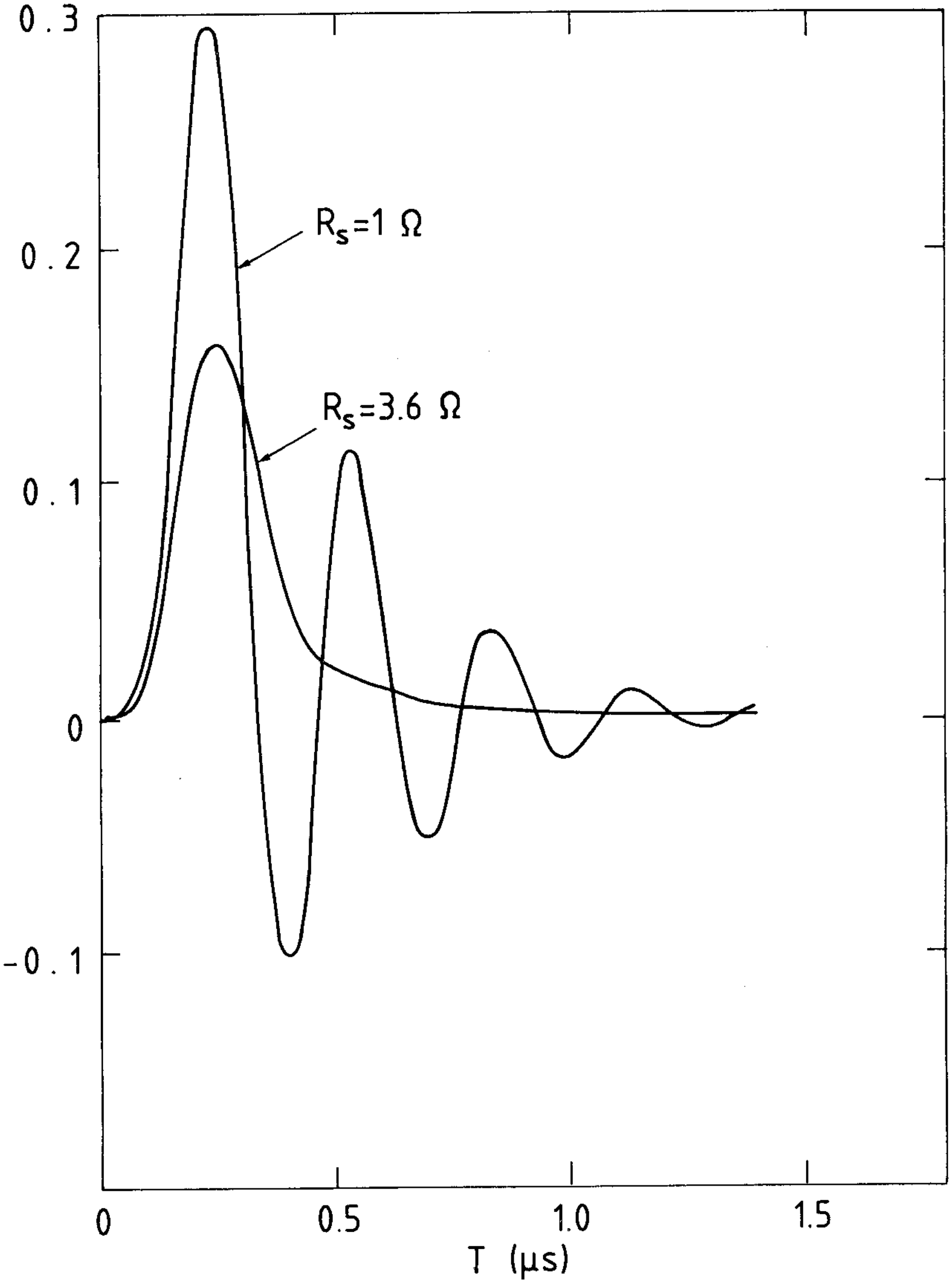

fig. 16b

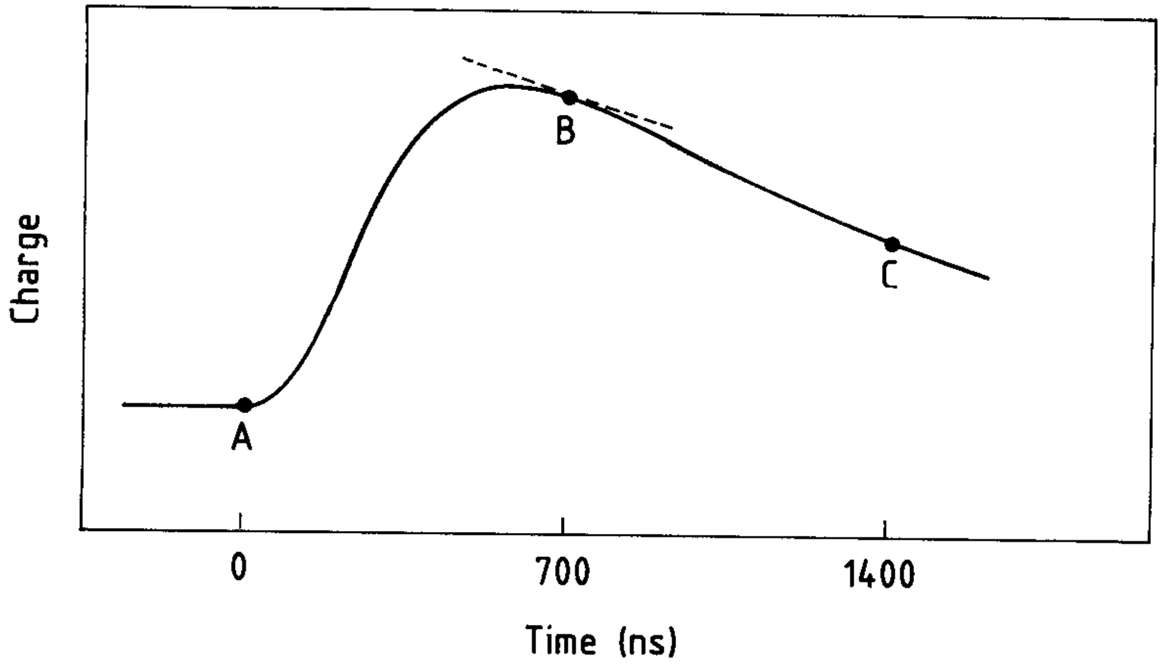

Measured charge $Q = (Q_B - Q_A) - (Q_C - Q_B)$

fig. 17a

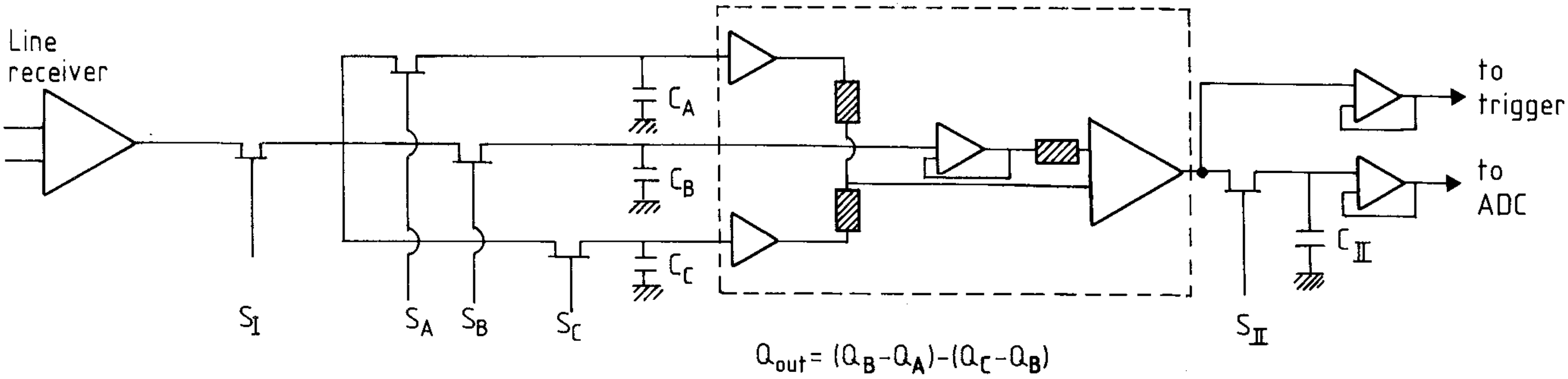
Line receiver
S_I
S_A
S_B
S_C
C_A
C_B
C_C
$Q_{out} = (Q_B - Q_A) - (Q_C - Q_B)$
S_{II}
C_{II}
to trigger
to ADC

fig. 17b

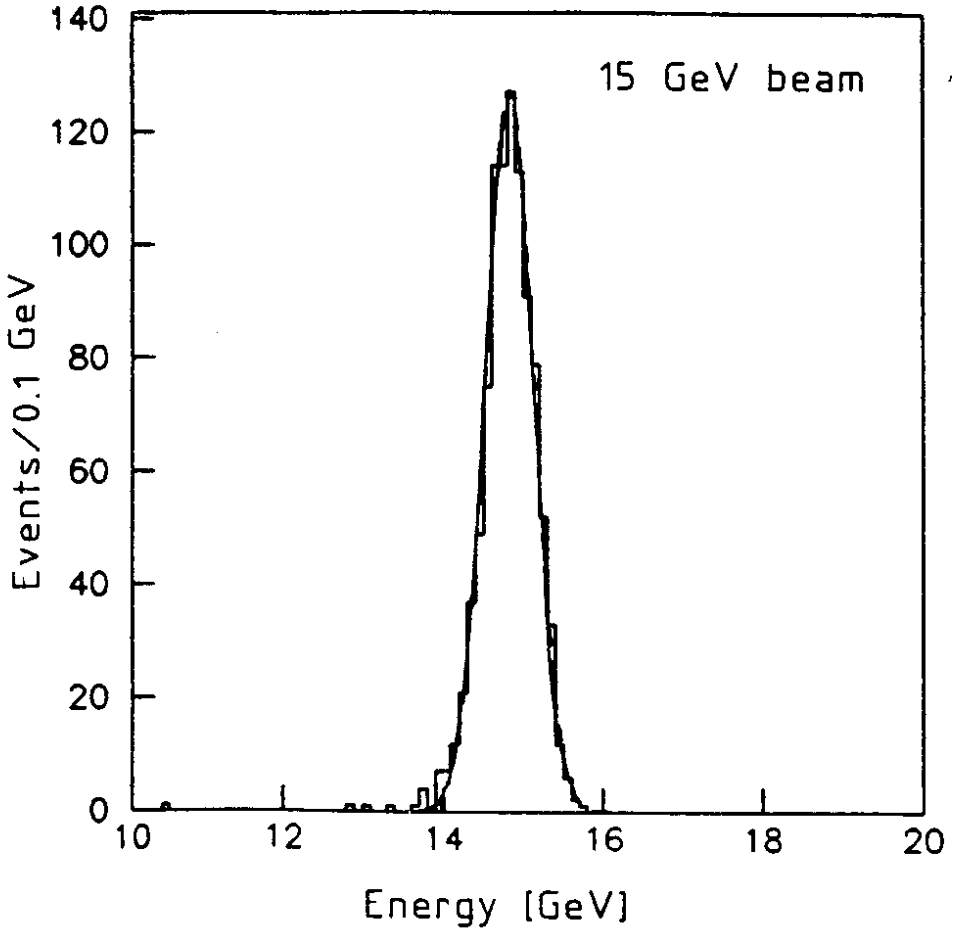

fig. 18a

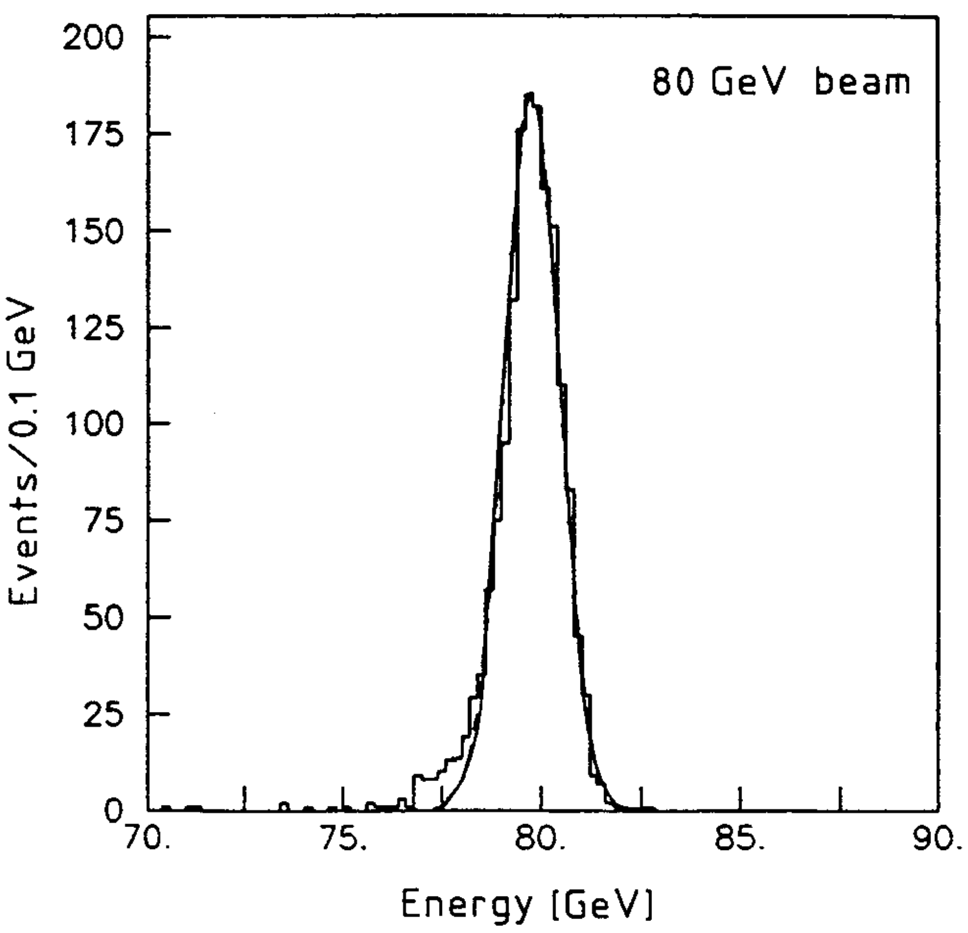

fig. 18b

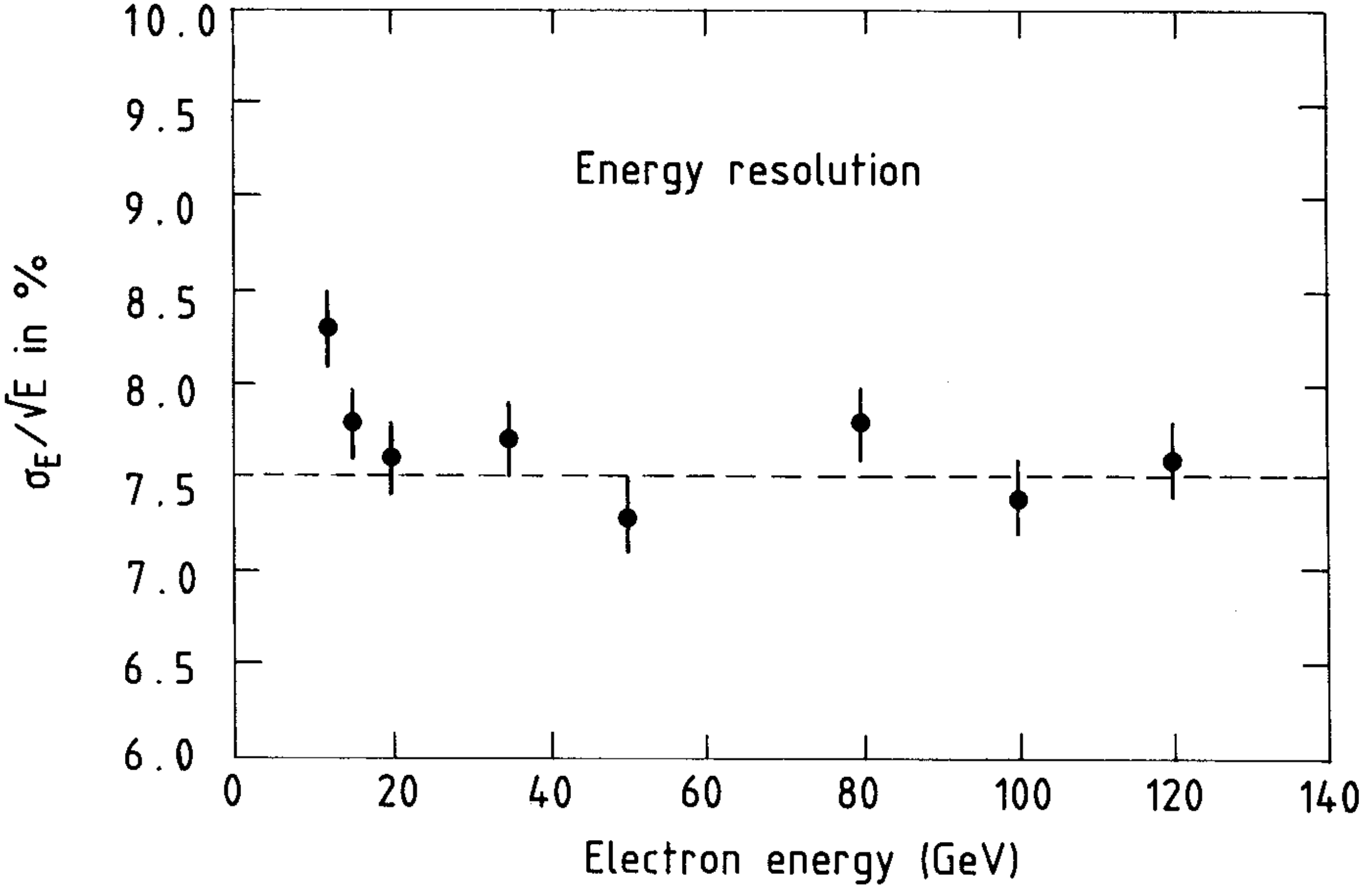
Energy resolution
$\sigma_E/\sqrt{E}$ in %
10.0
9.5
9.0
8.5
8.0
7.5
7.0
6.5
6.0
0
20
40
60
80
100
120
140
Electron energy (GeV)

fig. 19

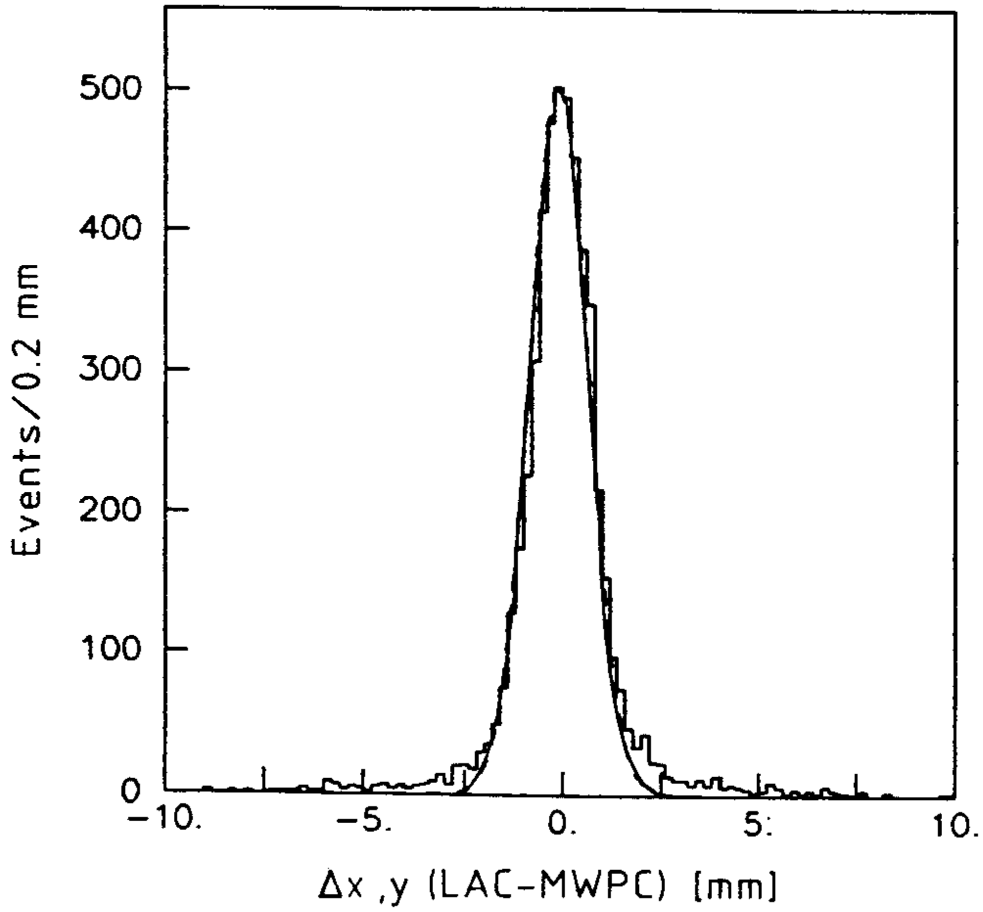

fig. 20

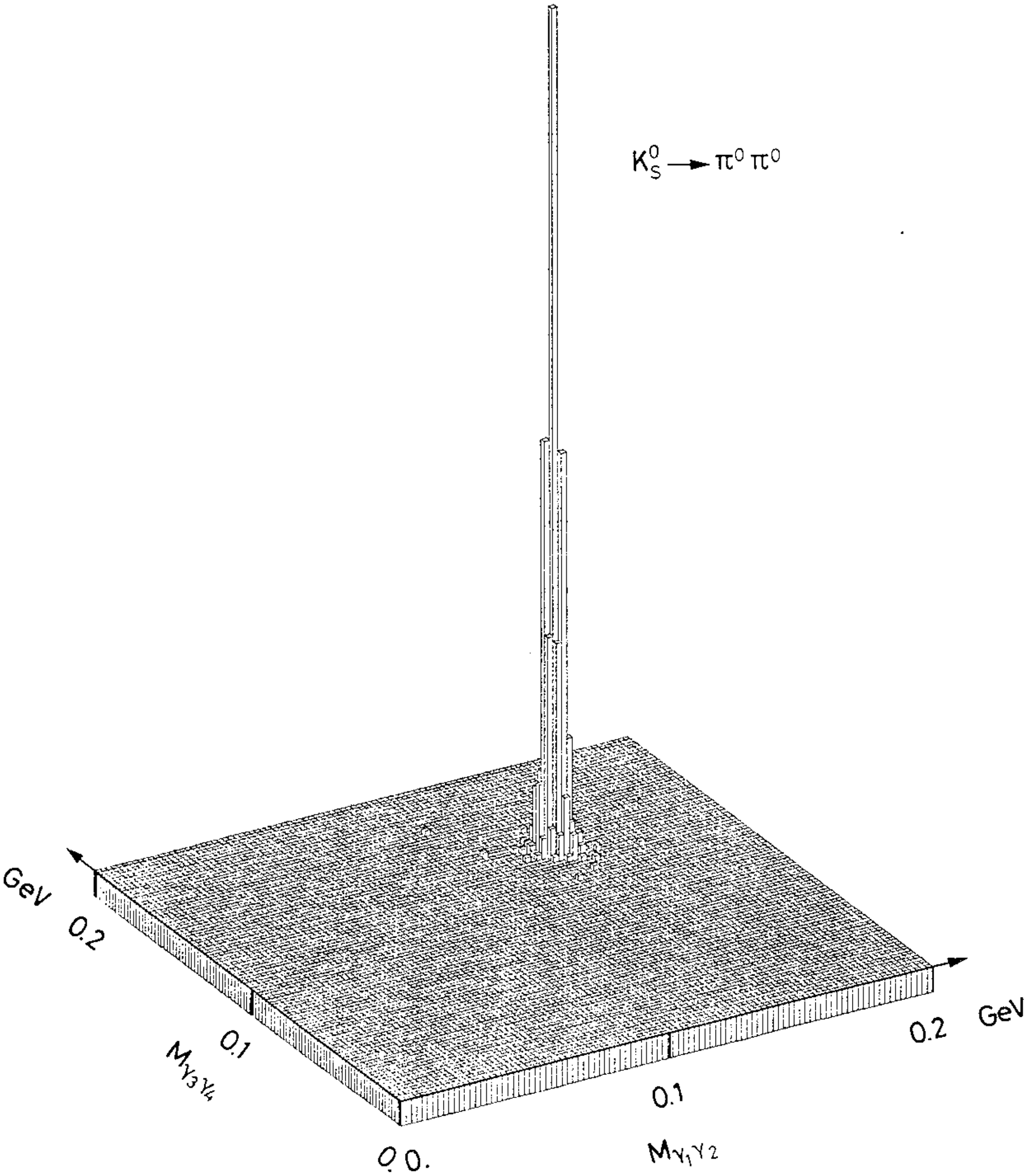
$K_S^0 \rightarrow \pi^0\pi^0$
GeV
0.2
0.1
$M_{\gamma_3\gamma_4}$
0.0.
0.1
0.2
GeV
$M_{\gamma_1\gamma_2}$

fig. 21

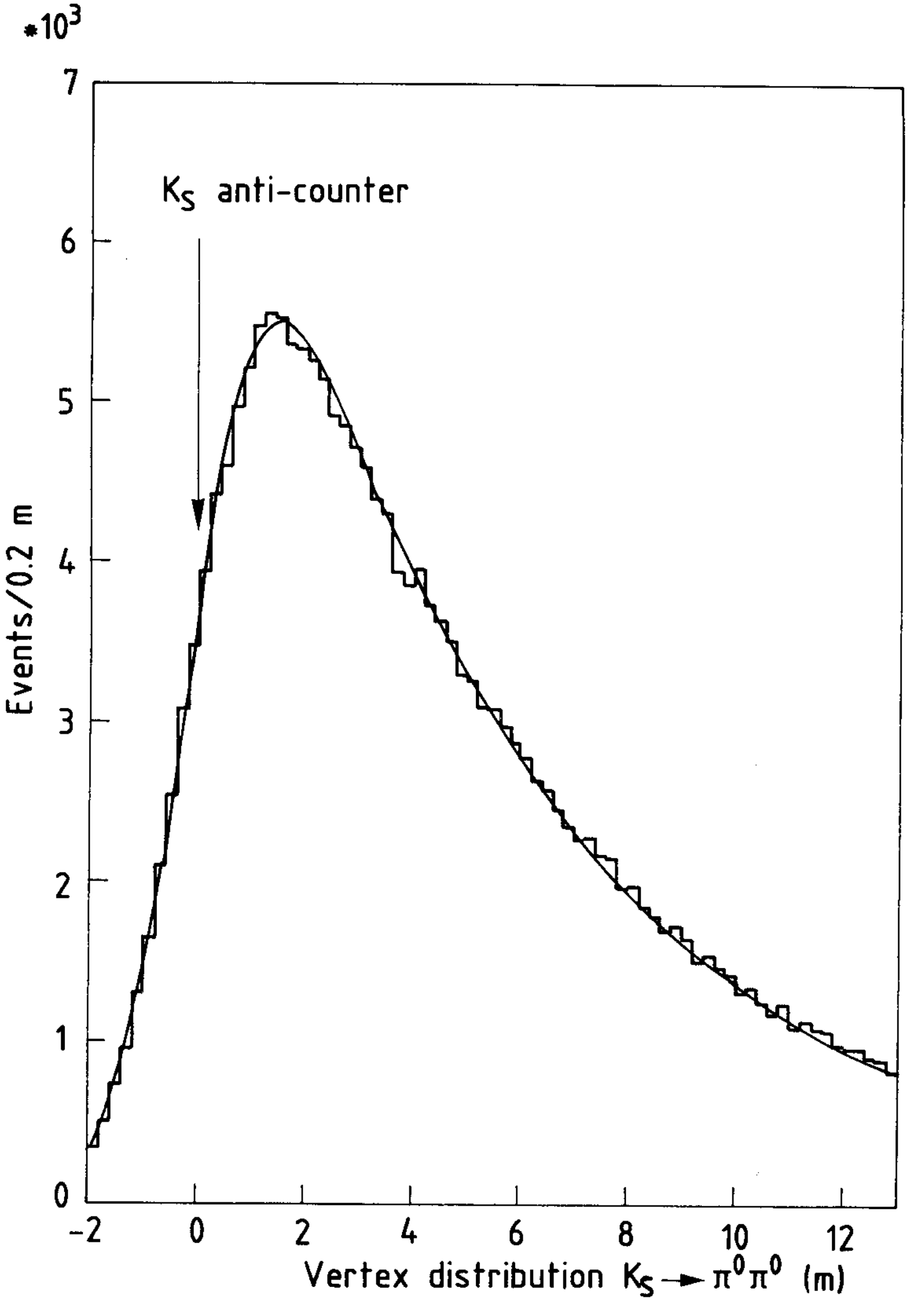
*10^3
7
6
5
4
3
2
1
0
Events/0.2 m
K_S anti-counter
-2
0
2
4
6
8
10
12
Vertex distribution K_S → π⁰π⁰ (m)

fig. 22

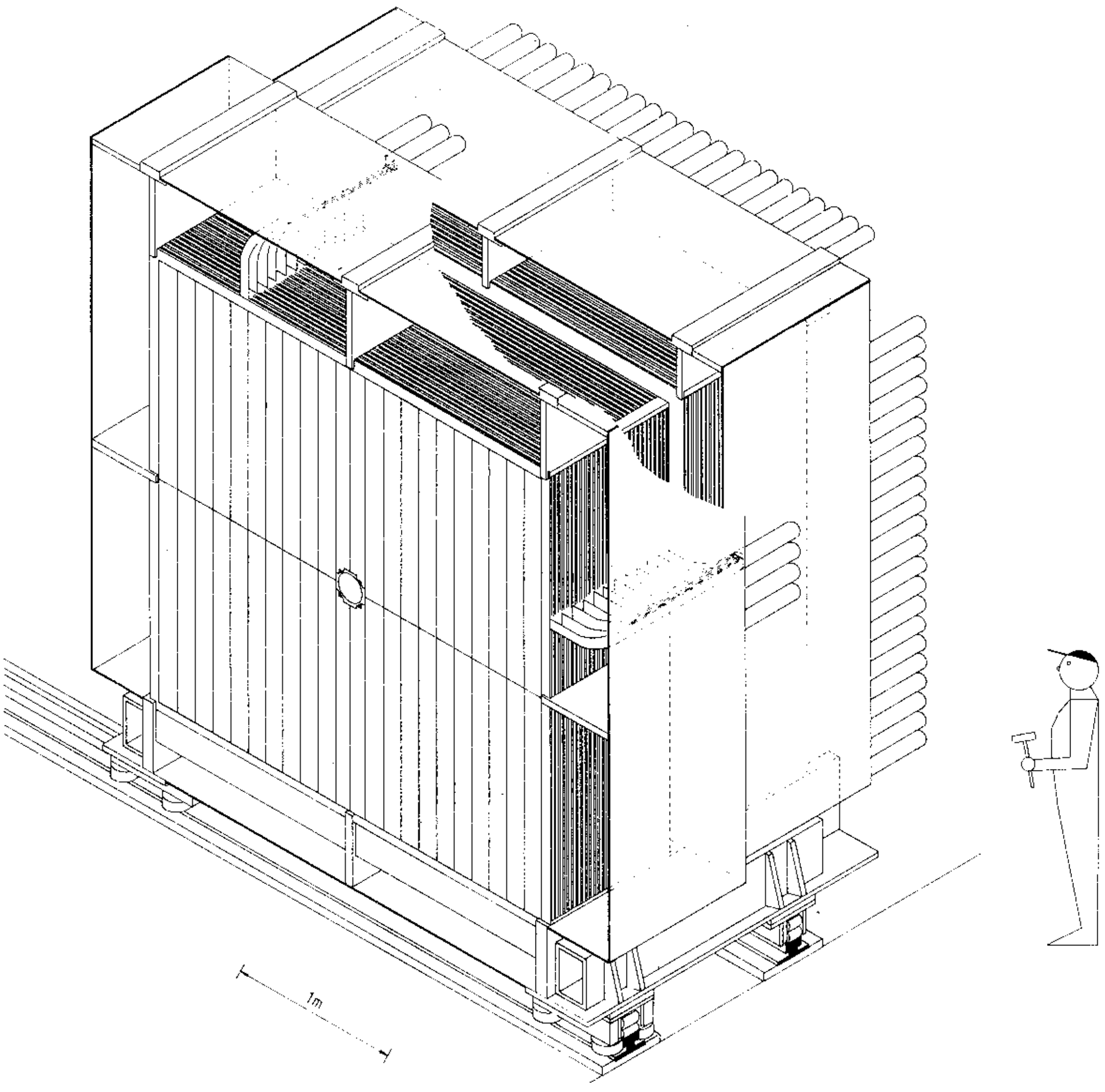

fig. 23

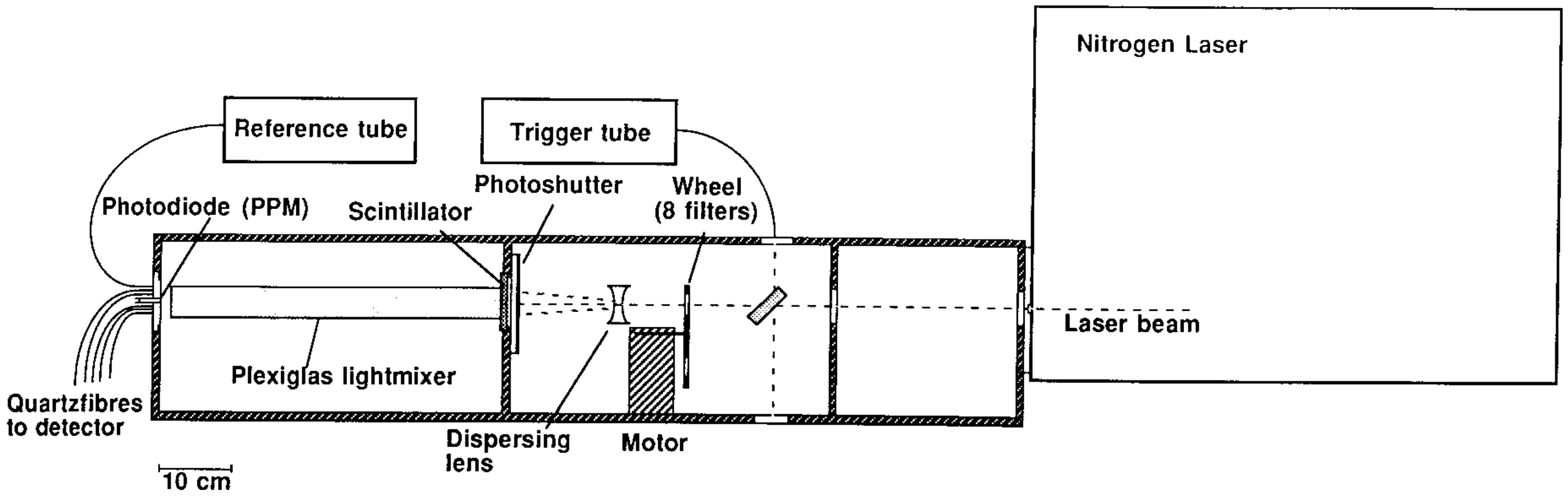
Reference tube
Trigger tube
Nitrogen Laser
Photodiode (PPM)
Scintillator
Photoshutter
Wheel
(8 filters)
Laser beam
Plexiglas lightmixer
Quartzfibres
to detector
Dispersing
lens
Motor
10 cm

fig. 24

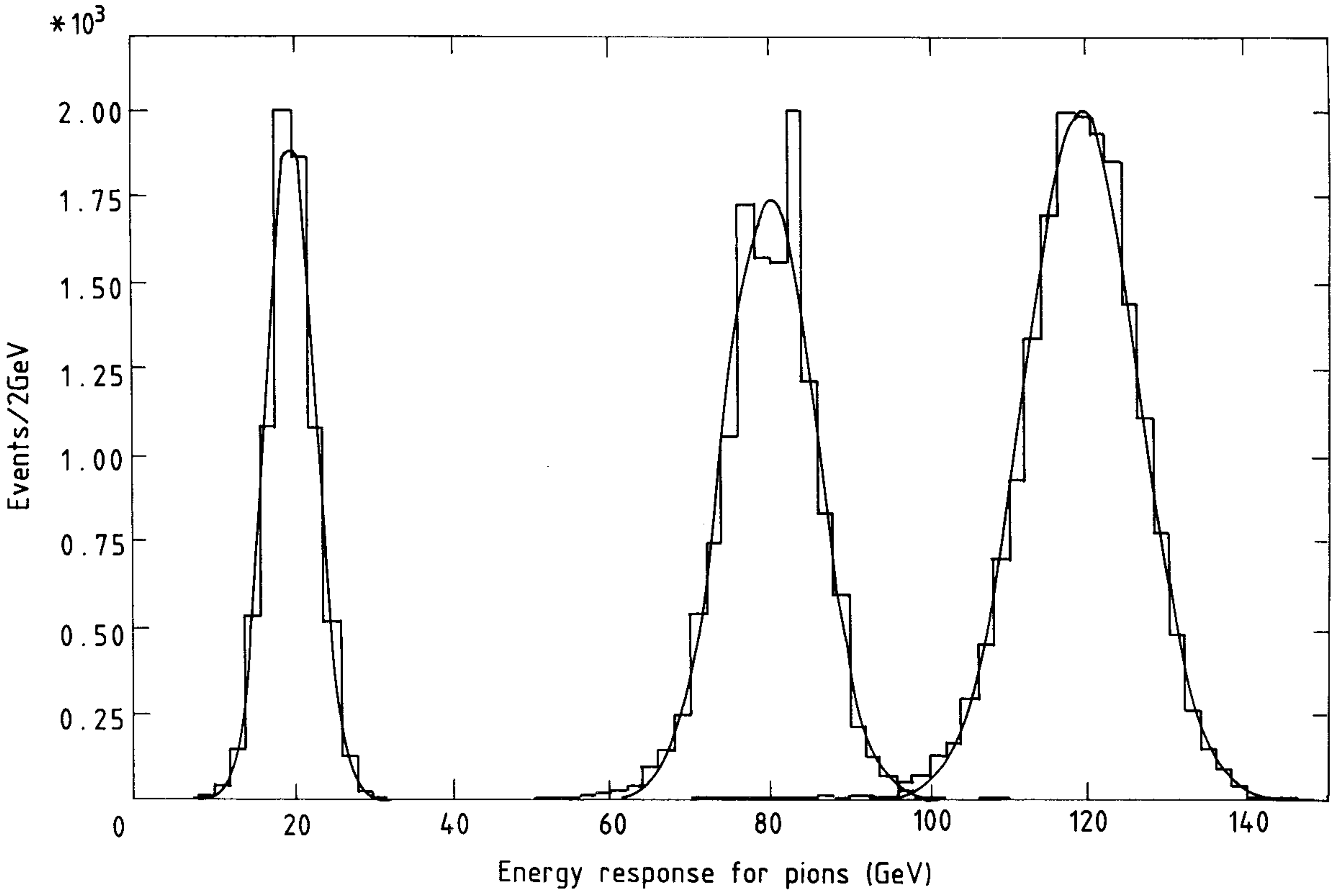
*10^3
2.00
1.75
1.50
1.25
1.00
0.75
0.50
0.25
Events/2GeV
0
20
40
60
80
100
120
140
Energy response for pions (GeV)

fig. 25

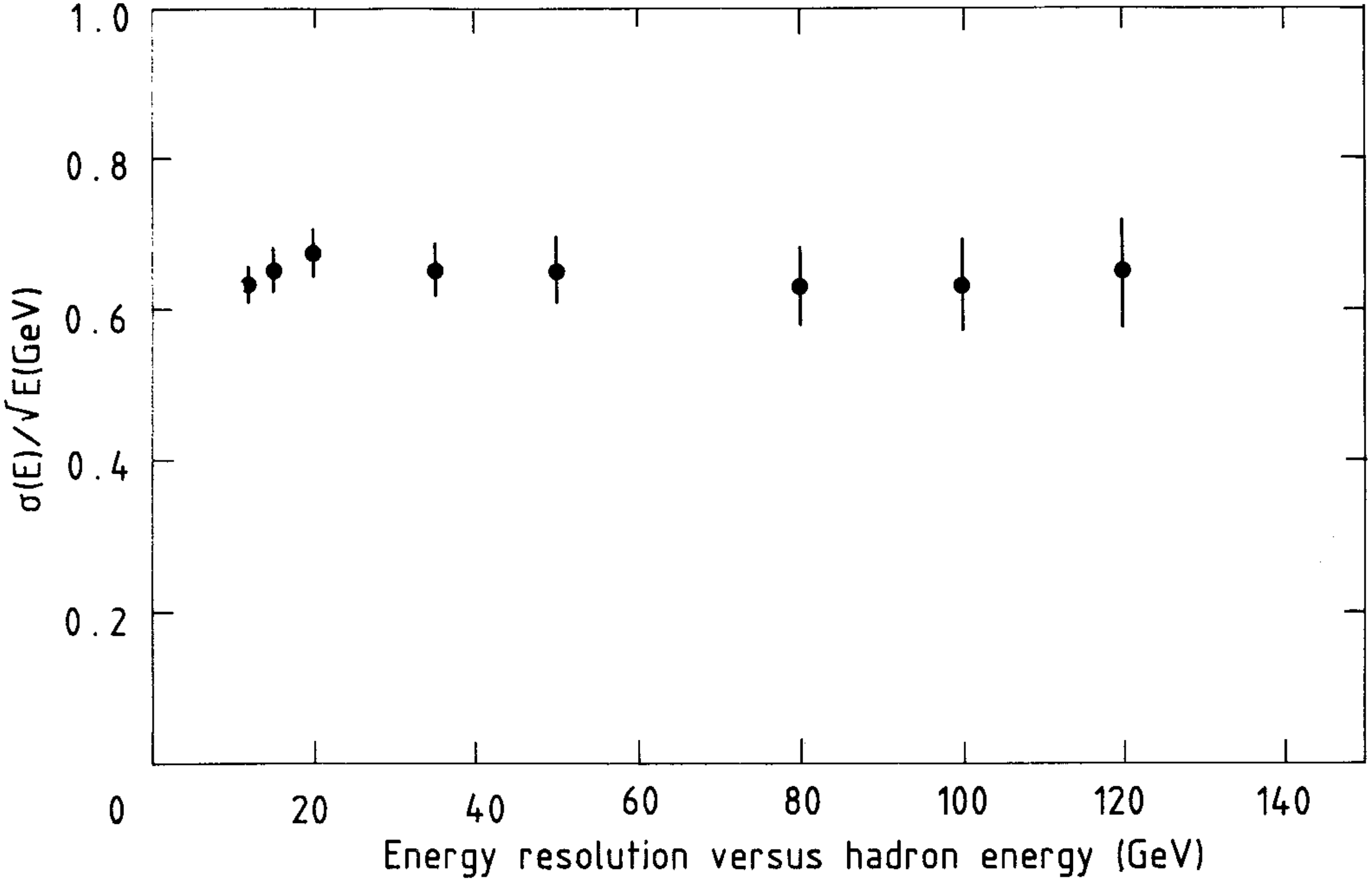
1.0
0.8
0.6
0.4
0.2
0
20
40
60
80
100
120
140
σ(E)/√E(GeV)
Energy resolution versus hadron energy (GeV)

fig. 26

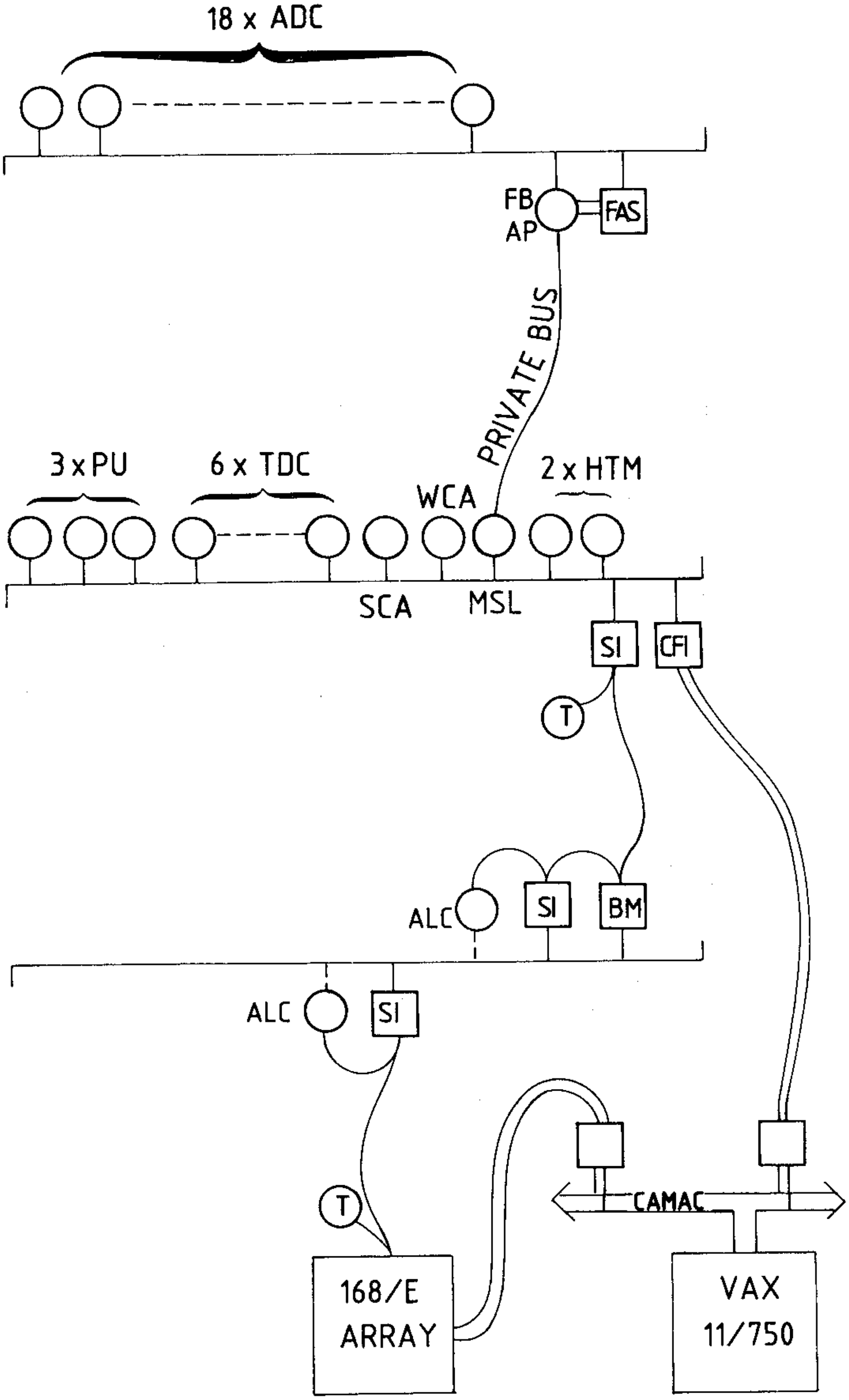

18 x ADC
FB
AP
FAS
PRIVATE BUS
3 x PU
6 x TDC
WCA
2 x HTM
SCA
MSL
SI
CFI
T
ALC
SI
BM
ALC
SI
CAMAC
T
168/E
ARRAY
VAX
11/750

fig. 27

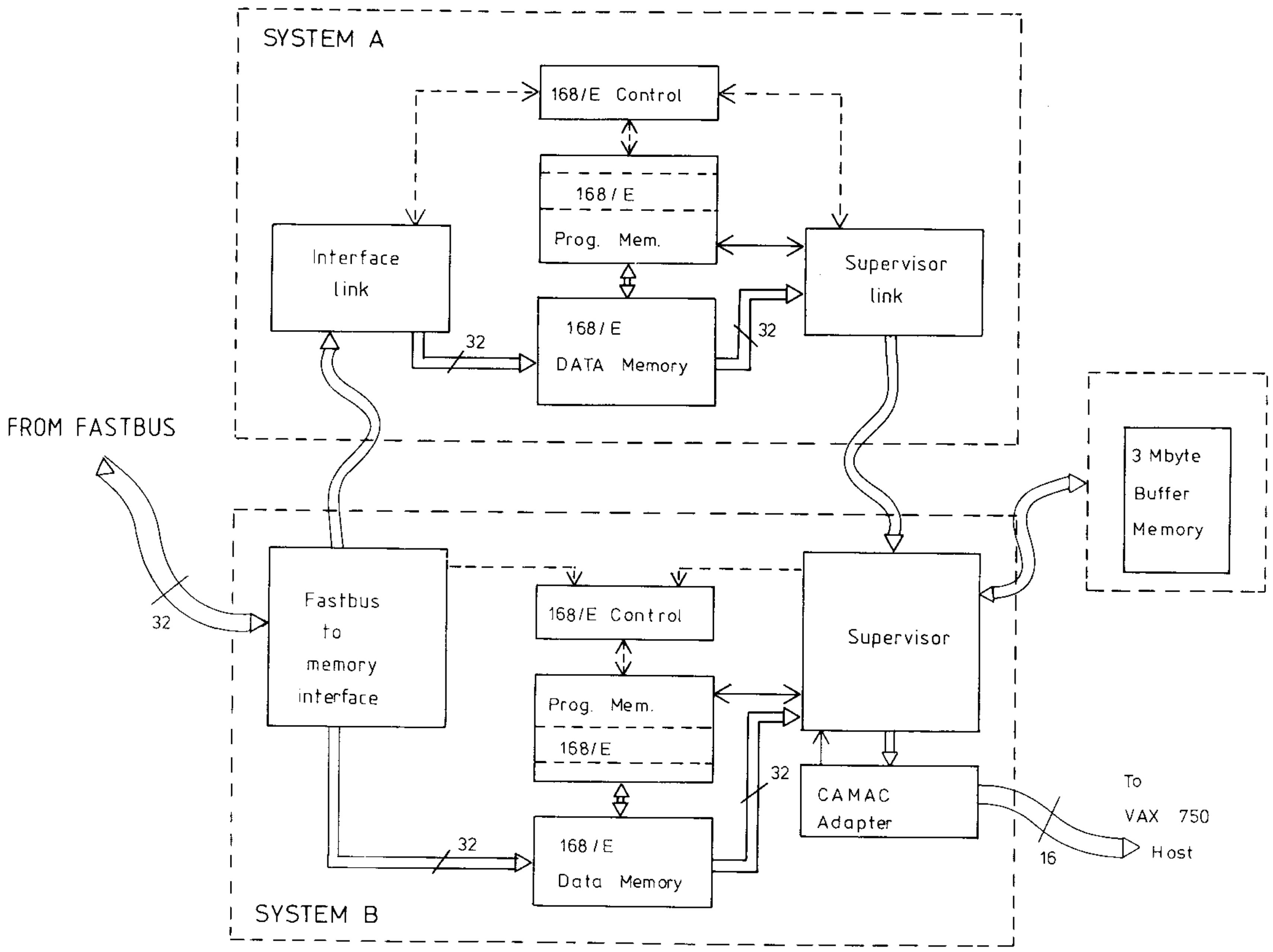
SYSTEM A
168/E Control
168/E
Prog. Mem.
Interface link
Supervisor link
32
168/E DATA Memory
32
FROM FASTBUS
32
3 Mbyte Buffer Memory
Fastbus to memory interface
168/E Control
Supervisor
Prog. Mem.
168/E
32
CAMAC Adapter
To VAX 750 Host
16
32
168/E Data Memory
SYSTEM B

fig. 28

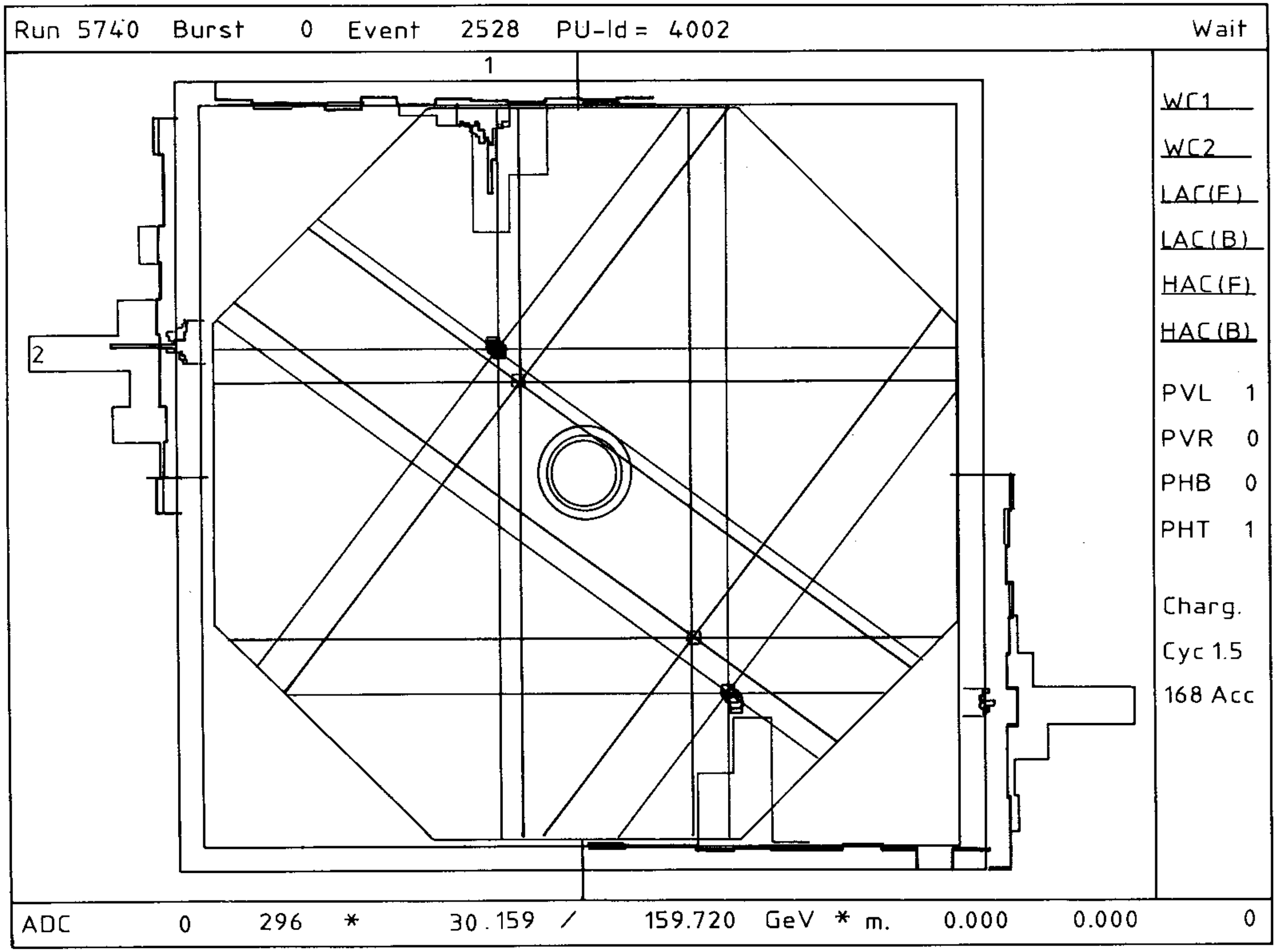
Run 5740 Burst 0 Event 2528 PU-Id = 4002
Wait
1
2
WC1
WC2
LAC(F)
LAC(B)
HAC(F)
HAC(B)
PVL 1
PVR 0
PHB 0
PHT 1
Charg.
Cyc 1.5
168 Acc
ADC 0 296 * 30.159 / 159.720 GeV * m. 0.000 0.000 0

fig. 29a

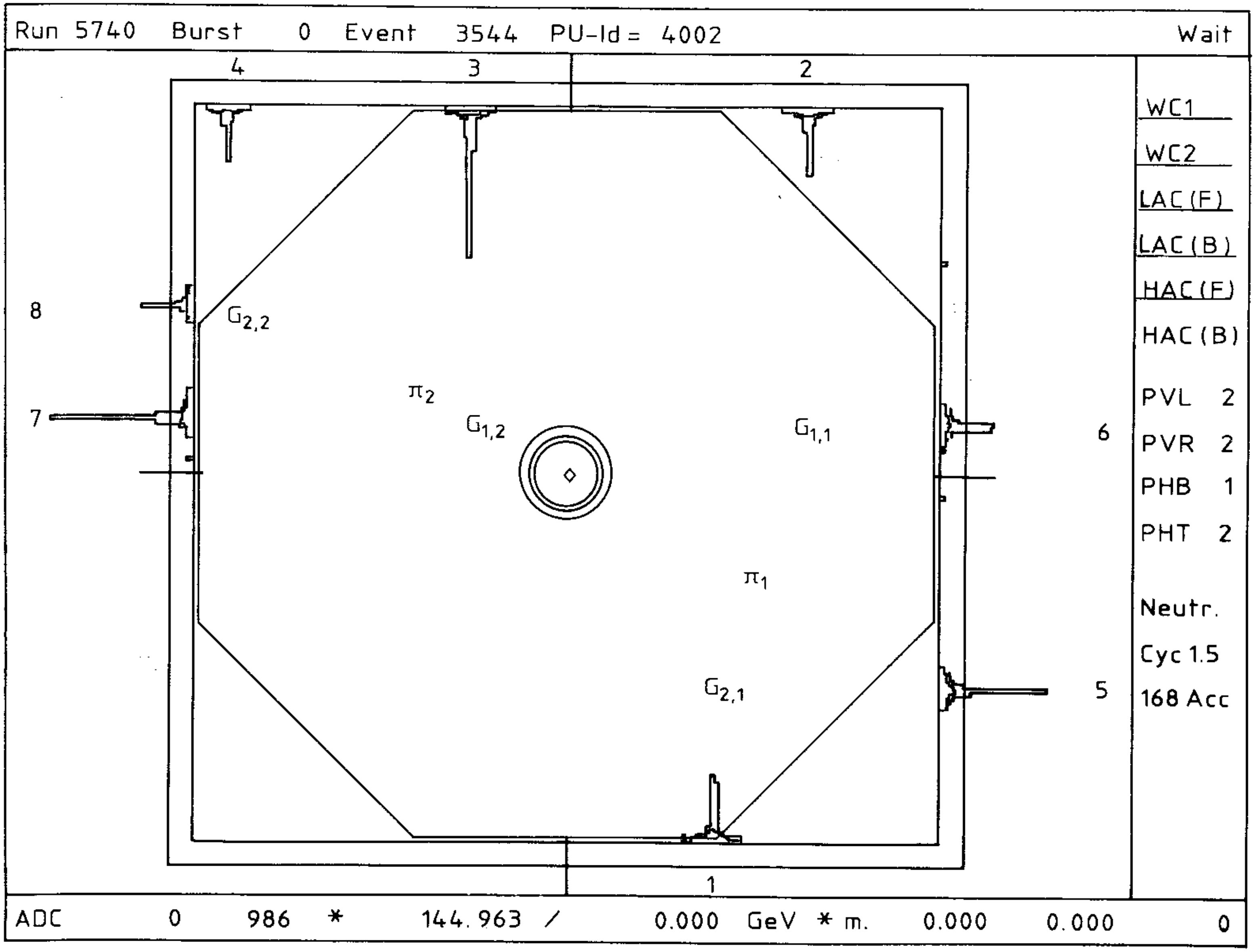
Run 5740 Burst 0 Event 3544 PU-Id = 4002
Wait
WC1
WC2
LAC(F)
LAC(B)
HAC(F)
HAC(B)
PVL 2
PVR 2
PHB 1
PHT 2
Neutr.
Cyc 1.5
168 Acc
1
2
3
4
5
6
7
8
$G_{2,2}$
π_2
$G_{1,2}$
$G_{1,1}$
π_1
$G_{2,1}$
ADC 0 986 * 144.963 / 0.000 GeV * m. 0.000 0.000 0

fig. 29b